Summer 2020

The Structural and Magnetic Properties of NiO/Mn(Ni)-Oxide Magnetic Heterostructured Nanocrystals Synthesized Under Varying pH Values

Abdullah Al Shafe
Missouri State University, Shafe400@live.missouristate.edu

THE STRUCTURAL AND MAGNETIC PROPERTIES OF NIO/MN(NI)-OXIDE MAGNETIC HETEROSTRUCTURED NANOCRYSTALS SYNTHESIZED UNDER VARYING PH VALUES

A Master's Thesis

Presented to

The Graduate College

Missouri State University

In Partial Fulfillment

Of the Requirements for the Degree

Master of Science, Materials Science

By

Abdullah Al Shafe

August 2020

THE STRUCTURAL AND MAGNETIC PROPERTIES OF NIO/MN(NI)-OXIDE MAGNETIC HETEROSTRUCTURED NANOCRYSTALS SYNTHESIZED UNDER VARYING PH VALUES

Physics Astronomy and Materials Science

Missouri State University, August 2020

Master of Science

Abdullah Al Shafe

ABSTRACT

The role of pH on the structural, morphological, and magnetic properties of hydrothermally synthesized NiO-based magnetic heterostructured nanocrystals (MHNCs) is investigated. The NiO nanocrystals were synthesized using a two-step thermal decomposition process whereas the deposition of the surrounding Mn-based phases was accomplished by hydrothermal means at pH values ranging from 2.4 to 7.0. The resulting heterostructured nanocrystals consist of inverted AFM-FiM NiO/±$Mn_xNi_{1-x}O$/±Mn_3O_4 bimagnetic/trimagnetic systems. A complete characterization of the MHNCs was carried using XRD, TEM, EDS, MPMS magnetometry and XPS analysis. Structural investigations revealed predominantly faceted MHNCs ranging in size from 24-30 nm with expitaxially grown $Mn_xNi_{1-x}O$ overlayers and/or Mn_3O_4 decorated nanoislands. Magnetic data reveal a significant enhancement in the coercivity, exchange bias and remanent magnetization values with increasing pH values and peaking at a pH of ~5, followed by a substantial decline with further increasing pH. The XRD, TEM and magnetometry data are consistent with predominantly $Mn_xNi_{1-x}O$ shell formation at lower pH, mixed deposition of $Mn_xNi_{1-x}O$ shell and Mn_3O_4 islands at intermediate pH, and deposition of predominantly Mn_3O_4 islands at higher pH values. Finally, the XPS spectra analysis confirm Mn^{2+} incorporation at low pH values and an admixture of Mn^{2+} and Mn^{2+} at higher pH values in the MHNCs.

KEYWORDS: magnetic heterostructured nanocrystals, hydrothermal, pH, exchange bias, coercivity, magnetic domain, spinel structure, magnetic anisotropy, interface, XPS.

THE STRUCTURAL AND MAGNETIC PROPERTIES OF NIO/MN(NI)-OXIDE MAGNETIC HETEROSTRUCTURED NANOCRYSTALS SYNTHESIZED UNDER VARYING PH VALUES

By

Abdullah Al Shafe

A Master's Thesis
Submitted to the Graduate College
Of Missouri State University
In Partial Fulfillment of the Requirements
For the Degree of Master of Science, Materials Science

August 2020

Approved:

Robert A. Mayanovic, Ph.D., Thesis Committee Chair

Kartik C. Ghosh, Ph.D., Committee Member

Tiglet Besara, Ph.D., Committee Member

Julie J. Masterson, Ph.D., Dean of the Graduate College

ACKNOWLEDGMENTS

First of all, I am grateful to my advisor to Dr. Robert A. Mayanovic for granting me a position in his research group. I feel fortunate that I had the supervision of him in completing my research. His exemplary guidance, constant encouragement, and careful monitoring throughout my degree program are so great that even my profound gratitude is not enough. I would like to express my special thanks to Dr. Karthik C. Ghosh and Dr. Tiglet Besara for their continuous support and guidance throughout my journey at Missouri State University. I would also like to extend my gratitude to Dr. Ridwan Sakidja, Dr. Mourad Benamara from the University of Arkansas and Dr. Vladimir Roddatis from Germany for providing me with all the information, facilities and guidance that was required. Special thanks to other faculties and staff of the department of PAMS for their suggestions and help.

My completion of this thesis could not have been possible without the help of my colleagues – fellow graduate students. Especially my neighbors and students from Bangladesh - you guys are the best. Best of luck with your future endeavors. Thanks to my parents and siblings for always be appreciative and patient to me.

Finally, to my caring, loving and supportive wife, Sabila Kader Pinky, my deepest gratitude. It was great comfort and relief to have you always at my side. This thesis is dedicated to you.

TABLE OF CONTENTS

LIST OF TABLES

LIST OF FIGURES

CHAPTER 1: INTRODUCTION

Nanocrystal synthesis and characterization have been a fundamental component of modern nanomaterials and nanotechnology studies. Over the years, the diversity in nanocrystals has attracted researchers for exploring their novel and unique properties and their potential applications in various sectors of science. Nanocrystals are one kind of nanomaterials which can be considered as an aggregate of molecules having a length of 1 to 100 nm in at least one dimension [1]. Their properties lie between the bulk materials and molecules. The nanocrystals can be classified based on their size, shape, and applications. Among all kinds of nanocrystals, the most widely studied ones are semiconductor nanocrystals, magnetic nanocrystals, nanocrystal solar cells, quantum dots and nanoparticles [2]–[5]. On the other hand, a heterostructured nanocrystal (HNC) can be considered one kind of nanomaterial having multiple layers on top of one another connected by some interface [6]. A lot of studies have been done on heterostructured nanomaterials over the decades because of their promising physical, optical and electrical properties [6]–[10]. The layers in the structure are allowed to grow either as a natural phenomenon or artificially. Heterostructured nanocrystals (HNCs) can be grown either by sequential or concurrent or direct growth of different building blocks. But whatever the growth technique, the main mechanism of synthesis is the nucleation and growth of different material sections. Because of different layers in the structure, there can be intertwining or periodicity of properties which combined can introduce novel characteristics that do not occur naturally. The HNCs can be classified based on their dimensions as it is a conjugate of two or more distinctive nanomaterials. Figure 1.1 shows the classification of heterostructured nanocrystal based on the dimension.

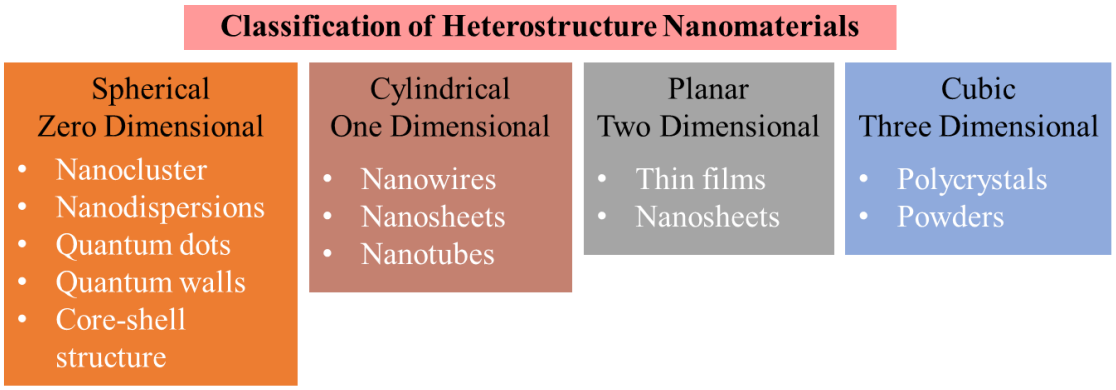

Figure 1.1: Classification of heterostructure nanomaterials

Figure 1.2(a) shows different combinations of the coating layer or depositions over the core of a 3-dimensional particle-like heterostructured nanocrystal. As can be seen from the picture, there can be two types of growth of the coating layer – (i) epitaxial and (ii) nonepitaxial. Epitaxial growth covers the fact that the newly grown coating layer can have the same crystal structure as the core called homoepitaxy or a different structure called heteroepitaxy [11]. Figure 1.2(a) also shows the nonepitaxial growth which means the grown material does not depend on the structure of the core material and it can have a different crystal structure and shape [12]. Figure 1.2(b) and 1.2(c) illustrate some more forms of the heterostructured nanocrystals where it does not only take a particle-like shape rather rod-like structure called nanorod and nanowire. Nanorods and nanowires are other forms of MHNCs that have been studied extensively by various researchers [13]–[16]. They can be transformed into excellent magnetic heterostructured nanocrystals and can provide enhanced magnetic and electrical properties [15]. The increased amount of surface plasmon excitations occurs in nanorods and nanowires due to the larger aspect ratio which amplifies the electrical field of the total structure. One important difference between epitaxial and nonepitaxial growth of the coating layer is the lattice mismatch. Since nonepitaxial

growth maintains a different crystal structure, there can be a lot of lattice mismatch between the two structures. Apart from the lattice mismatch, there can be other surface defects such as vacancy, surface roughness as well at the interface of the structures. Figure 1.3 shows the transmission electron microscopy (TEM) image of a system where structural uniformity is maintained at the interface in both of the images but – (a) has only $Mn_xNi_{1-x}O$ shell which is called homoepitaxy and (b) has both $Mn_xNi_{1-x}O$ shell Mn_3O_4 islands termed as heteroepitaxy. In our study, we have synthesized faceted shaped [Figure 1.2(d)] and pseudo-spherical type [Figure 1.2(e)] MHNCs out of which some are inverted core-shell type nanocrystals and some are multiple layered having both shell and nanoislands.

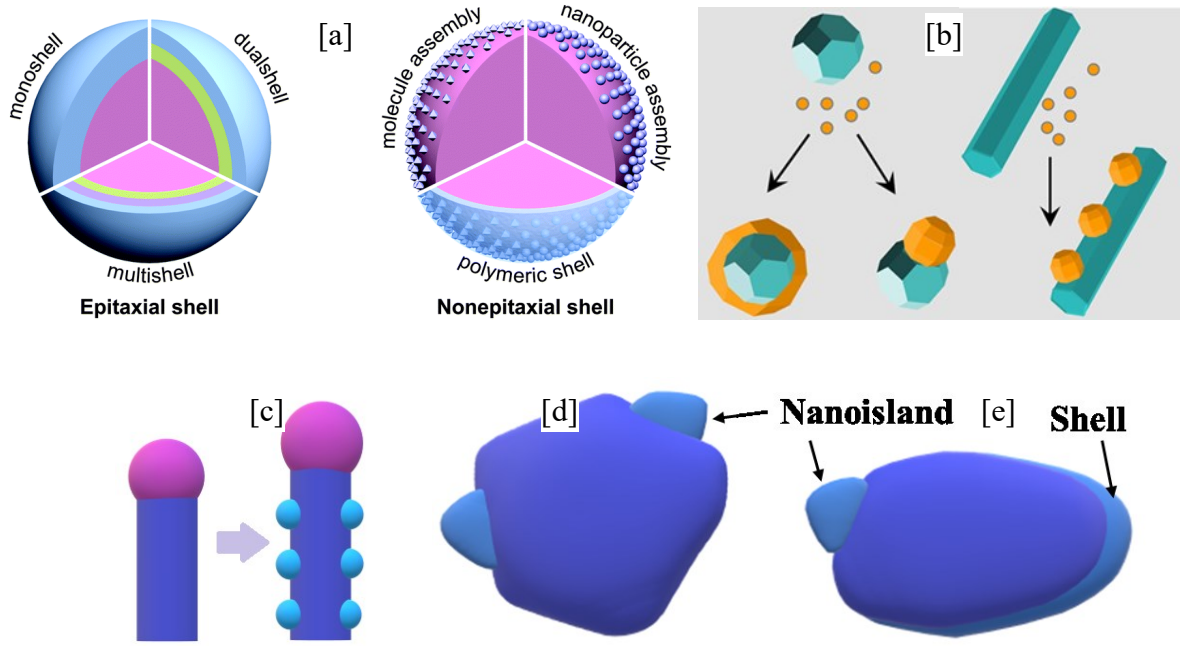

Figure 1.2: (a) Different combinations of coating layers on heterostructured nanocrystals [17], (b) deposition of secondary layer over primary nanomaterial in different possible forms [18], (c) nanowires and deposition on nanowire (d) faceted nanostructure having nanoislands as depositing layer (e) pseudo-spherical structure having both shell and nanoislands

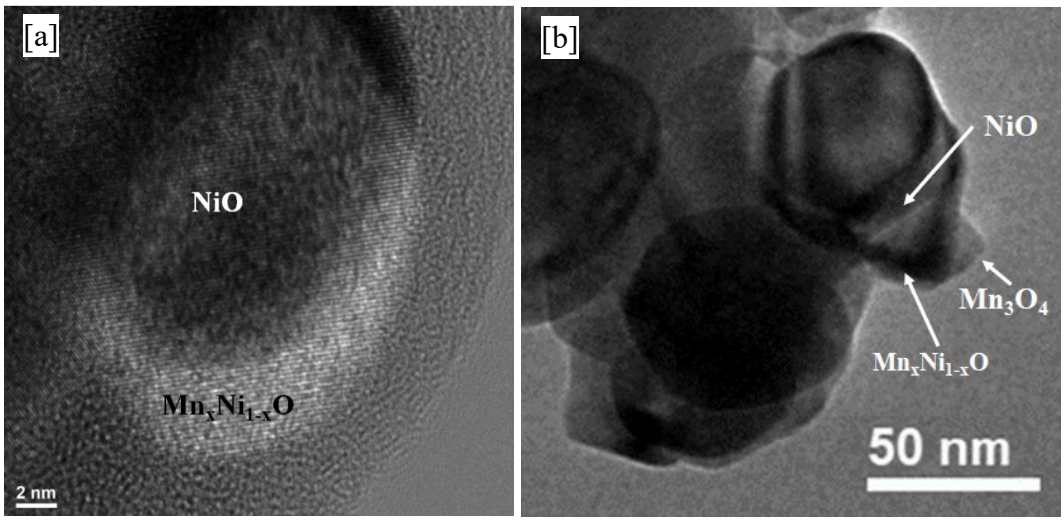

Figure 1.3: (a) Homoepitaxial growth of $Mn_xNi_{1-x}O$ shell Mn_3O_4 islands over NiO core (b) heteroepitaxial growth of both $Mn_xNi_{1-x}O$ shell and Mn_3O_4 islands over NiO core.

Bimagnetic heterostructured materials refer to the combination of either a hard/soft or soft/hard magnetic materials system. They are particularly investigated because of their complex structure that can provide controllable magnetic properties. The system having hard magnetic material as the core surrounded by the soft material is called normal core-shell structure while the reverse is called inverted core-shell structure. There can be multiple layers of shells such as shell-core-shell or core-shell-shell for bimagnetic structure. The combination of soft/hard and hard/soft nanomaterials connected by direct interfaces in a bimagnetic system can introduce large exchange bias, tunable blocking temperature, high susceptibility and excellent coercivity [19]–[21]. The magnetic properties of soft magnetic layers are highly influenced by the hard magnetic layer in a bimagnetic system. For example, the magnetization distribution in the soft components of bimagnetic materials is altered by the magnetostatic hard/soft coupling and changes caused by the hard component [22]. But it is still unclear how the stoichiometry gradient, interface diffusion, crystalline and surface disorder affect the magnetic response in the bimagnetic

structure. It has been established that in an AFM/FiM or AFM/FM inverted core/shell type structure, it is easier to control the hard AFM magnetic layer because the shell deposits in less favorable condition compared to the core [20]. In our present work, we have synthesized NiO based magnetic heterostructured nanocrystals (MHNCs) with NiO as the core and manganese oxide as the coating and/or depositing layer in any other form such as nanoislands. As both NiO and MnO is a hard AFM type material and various oxides of manganese (Mn_3O_4, $Mn_xNi_{1-x}O$, MnOOH) are soft magnetic material, we have referred the system as a bimagnetic heterostructure nanocrystal [23], [24]. We have investigated their physical, compositional and magnetic properties to understand the interface dependent magnetic properties, interactions with different layers and the morphological change with the growth of coating layers.

MHNCs have been investigated recently for their remarkable properties and potential for various applications. There have been a variety of combinations of magnetic heterostructured nanocrystals among which ferro-ferrimagnet, ferro-antiferromagnet, ferromagnet-semiconductor, ferromagnet-superconductor combinations are the most common ones [6][25]. These heterostructures of magnetic materials exhibit highly novel properties that may be useful for different sectors of engineering, medical applications, and space research [26][27][28]. Certain novel physical properties of MHNCs are due to their remarkable exchange bias (EB), interlayer exchange coupling, huge magneto-resistance and spin injection [25]. But most importantly, MHNCs have a large surface to volume ratio which makes them unique in comparison to their bulk counterparts. Because of this property, new functionality and performance have been achieved for MHNCs. As illustrated in Figure 1.4, the MHNCs have striking potentials for use in drug delivery, medical diagnosis, recording media, spintronic devices, ferrofluids, pigments and hyperthermia [26][29][30]. Krishnendu et. al. have shown that MHNCs can increase vascular

circulation lifetime and bioavailability which can result in increased efficacy and lesser dosage drugs [31]. MHNCs are also purported to be highly useful for targeted drug delivery systems and monitoring of drug release. The optical properties of MHNCs are particularly useful for diagnostic purposes as well as for imaging by the creation of organic dyes [31]. The MHNCs are also used in MRI contrast agents in place of conventional gadolinium-based contrast agents, magnetic RAM of insulator spintronic and GMR read heads in large capacity hard disk drives [31]. Akash et. al. have stated that MHNCs have benefits for use in spintronic devices, including miniaturization, nonvolatile memory, increased data processing speed and decreased power consumption [32]. MHNCs are particularly useful as they have fast switching times between spin states, which is important for miniature sized spintronic devices.

NiO has been investigated intensively for it's tunable structural, electrical and magnetic properties. Bulk NiO has a cubic (NaCl-type) rocksalt structure (Figure 1.5) at room temperature with a lattice parameter of 0.4177 nm and a wide band-gap ranging from 3.6 to 4.0 eV [33]. Nickel oxide is a strongly correlated material that exhibits insulating character and antiferromagnetic (AFM) order persisting at rather high temperatures; the Néel temperature of NiO is T_N = 523 K [33]. Magnetic properties of NiO nanoparticles are different from that of bulk NiO as they exhibit superparamagnetism and occasionally weak ferromagnetism: the latter property may be observed in very small nanostructures (< 5 nm) owing to the very large surface-to-volume ratio [34]. The superparamagnetism is due to the uncompensated spins present in the lattice structure occurring predominantly at the surface of the nanoparticles. The uncompensated spins can be highly useful in device applications due to their being pinned by the spins of any other ferromagnetic or ferrimagnetic materials. Thus the introduction of Ni^{2+} vacancies or

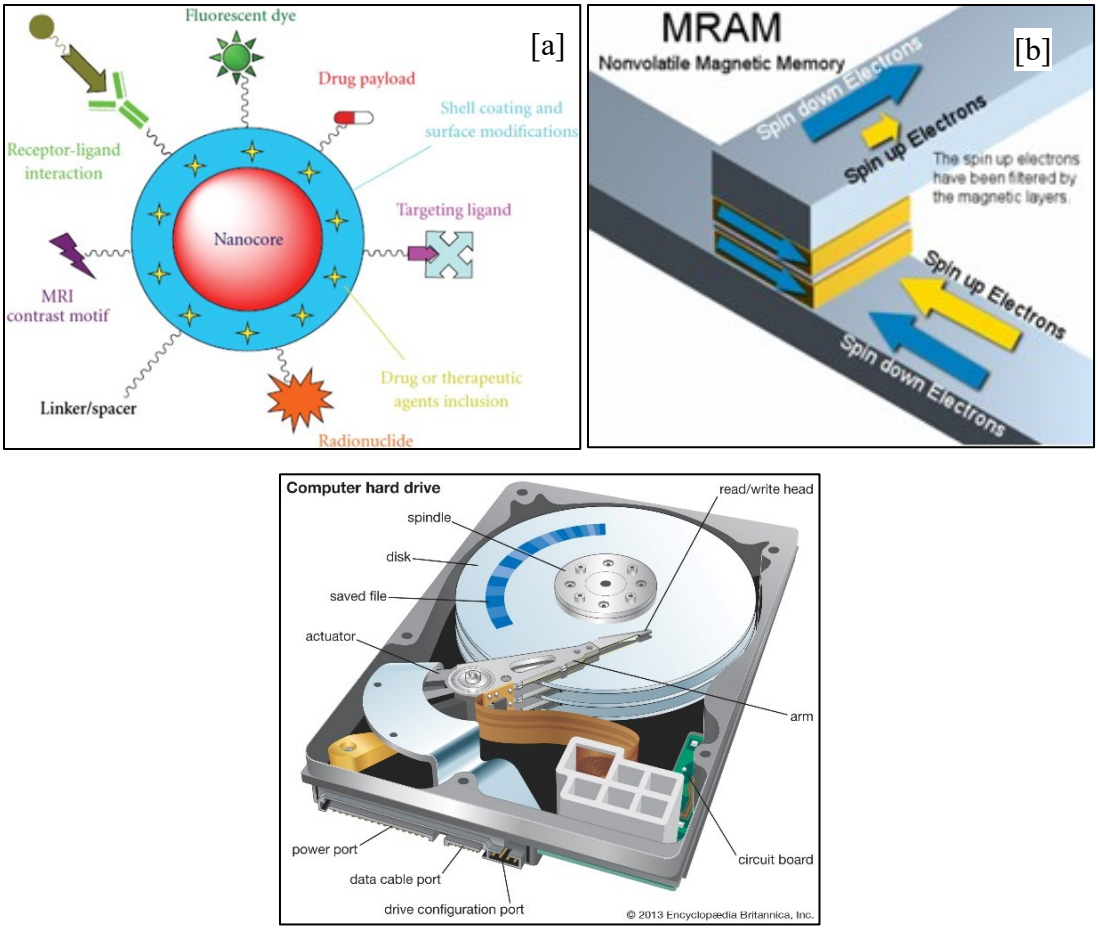

Figure 1.4: Applications of magnetic heterostructured nanocrystals in different sectors (a) drug delivery [6] (b) magnetic random access memory device [7] (c) read head in hard disk drive [35]

doping with other cations such as Fe^{2+}, Co^{2+}, or Mn^{2+} induces significant magnetic and electrical property change in NiO based heterostructured materials. Another explanation to this magnetism is - NiO has two non-local components of spin configurations because of the interaction between its nearest neighbors and next-nearest neighbors [36][37][38]. Both of the interactions are direct and strong which makes the ground state of NiO. If any of the Ni atoms are substituted by Mn, there will be a significant change in the spin orientation which might result in high magnetic properties. $Mn_xNi_{1-x}O$ is formed when Ni atoms are substituted for Mn atoms. Previous studies have shown that $Mn_xNi_{1-x}O$ also has the rocksalt type structure like NiO and has the same space

group of $Fm\bar{3}m$ [23]. That means crystal symmetry will be maintained if a $Mn_xNi_{1-x}O$ shell layer is grown over a NiO nanoparticle core. On the other hand, Mn_3O_4 (also called hausmannite) has a spinel structure with the space group *I*41/*amd*. Mn_3O_4 has both Mn^{2+} and Mn^{3+} ions occupying tetrahedral and octahedral sites, respectively, as shown in Figure 1.5 [39]. Mn^{2+} and Mn^{3+} ions that substitute for the Ni^{2+} ions have either larger (for the divalent state) or nearly the same (for the trivalent state) ionic radii of the ions (Ni^{2+} = 0.72 A, Mn^{2+} = 0.80 A, Mn^{3+} = 0.72 A). Thus, for Mn^{2+} substitution, a lattice expansion is expected for the rocksalt phase and, in the case of epitaxial growth, the NiO and $Mn_xNi_{1-x}O$ structures are not expected to match. In this case, crystal defects such as roughness, vacancy, lattice mismatch are expected along with the interface of these two phases.

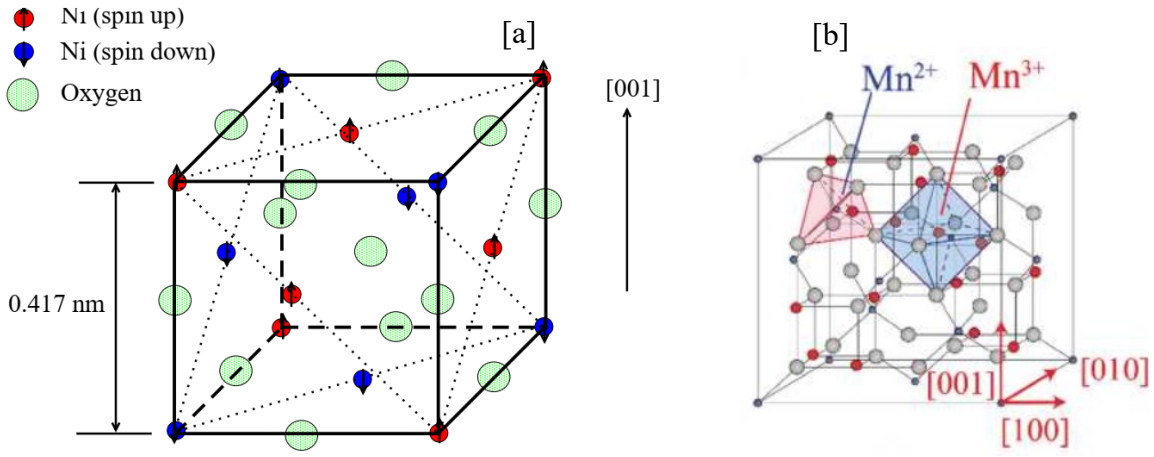

Figure 1.5: (a) NiO rocksalt structure (b) Mn_3O_4 spinel structure [39]

As stated earlier, bimagnetic heterostructured materials containing the AFM phase can introduce significantly large exchange bias. Since the invention of the exchange bias effect in 1956 by Meiklejohn and Bean of General Electric, this has been a breakthrough in the field of magnetism and device fabrication [40]. Much research effort over the years since the work of

Meiklejohn and Bean has gone into exploiting the exchange bias effect to make novel magnetic devices. The exchange bias (EB) is the most prominent example of coupling between different layers of ferro/ferrimagnetic and antiferromagnetic materials in a heterostructured system. It originates from the interfacial coupling effects between the surfaces of FM or FiM and AFM material due to uncompensated spins. It involves the pinning of the uncompensated spins of the FM or FiM layer along the same direction of the AFM layer, which typically controls the exchange bias. Although the net magnetization is due to the FM or FiM layer, the nature and strength of the EB are dictated by the properties of the AFM layer and the extent of the pinning of the spins in the interfacial region. The exchange bias field (H_E) is measured by the shift of the hysteresis loop in any direction (either positive or negative) with respect to the applied magnetic field.

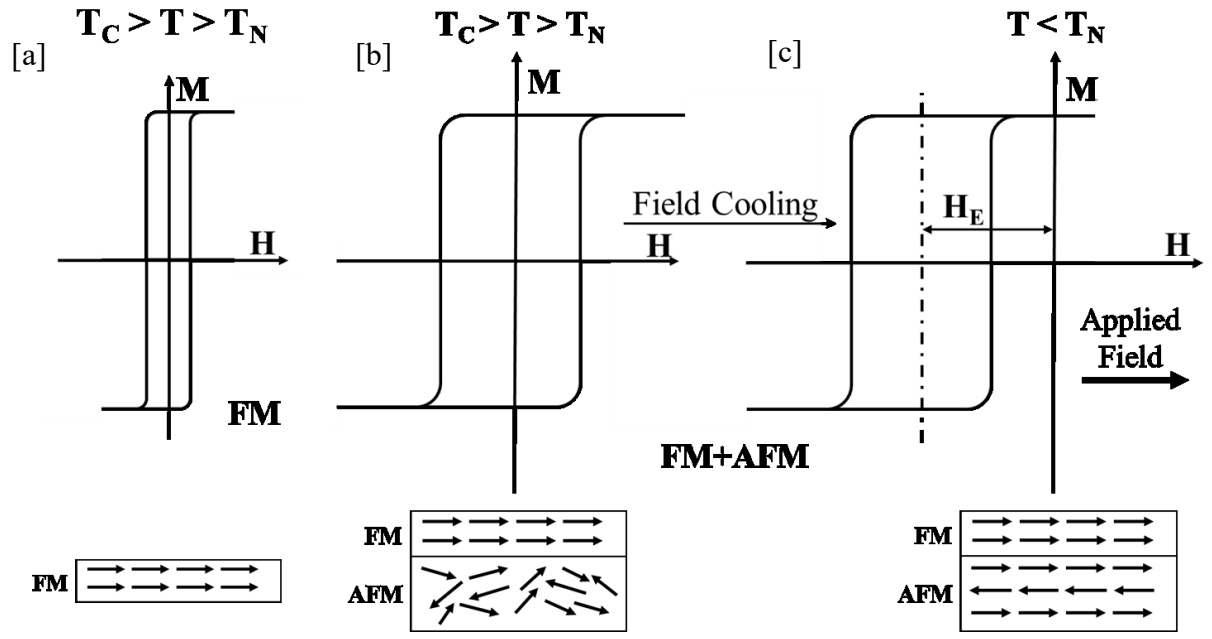

Figure 1.6: (a) A depiction of a typical M-H loop of ferromagnetic material and associated spin orientation (b) an M-H loop of combined FM-AFM bilayer and associated spin arrangement without the exchange bias, and (c) the same as in (b) but with the exchange bias in the FM-AFM bilayer at $T<T_N$

An easy axis in magnetism is the crystal direction in a system along which a small applied magnetic field is sufficient to reach the saturation magnetization (example: Ni has an <111> easy axis). Ferromagnetic materials have two equally favorable easy axes having the same energy. It is essential to provide the same amount of external field to rotate the magnetization of ferromagnetic materials from one easy direction to another by 180 degrees. That is why ferromagnetic materials show symmetry (magnetization, M vs magnetic field, H hysteresis loop) when there is no external applied field (Figure 1.6a). When the FM is joined with the AFM layer by a direct interface, the exchange coupling between them increases the coercivity of the total system (Figure 1.6b). The symmetry along the magnetic field remains the same for the total FM/AFM system. The spins in AFM are randomly distributed like in Figure 1.6(c). Upon the application of some externally applied field and at a temperature below the Néel temperature (T_N) of the AFM layer, the hysteresis loop will shift along the magnetic field direction. Here, T_C is the Curie temperature of the ferromagnetic layer. This shift along the magnetic field is defined as the exchange bias and direction of the shift reflects the fact that there is preferred magnetization direction for the FM layer now.

There are a couple of models to explain the basics of exchange bias. Some common models for exchange bias effects are the Stoner-Wohlfarth Model, the Meiklejohn, and Bean model, the Spin Glass (SG) model, the Random Field model (RF) of Malozemoff and the Domain State (DS) model [40]–[45]. Different models have been postulated over the years based on the numerical calculations and analytical expressions. These models have advantages over one another; for example, the Stoner-Wohlfarth model can explain the exchange bias effect for a large fraction of experimental data while it lacks the integrity to explain the coherent magnetization reversal [41]. The Meiklejohn model is one of the earliest models to explain the

magnetization reversal between FM and AFM spins and the effect of the interface on the coercivity [40], [42]. But one of the most ideal and recent models for exchange bias is the Spin Glass model which explains almost every aspect of the effect. The SG models consider the direct interface between FM and AFM phases and can explain the dependence of coercivity and exchange bias on the interface [43]. The SG model is also successful in explaining the effect of coating layer thickness on the coercivity and remanent magnetization behavior. Figure 1.7 depicts the ideal model (SG model) of the exchange bias effect.

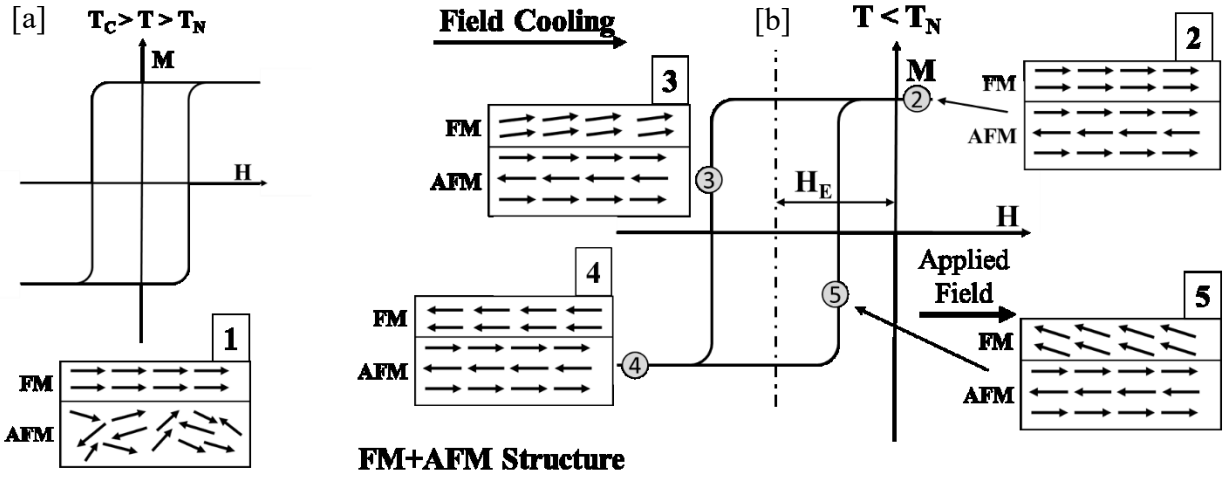

Figure 1.7: A schematic diagram showing an FM/AFM bimagnetic structure and the mechanism of exchange bias effects at a temperature below the Néel temperature (T_N) of the AFM layer [T_C = Curie temperature, H_E = exchange bias]. (a) The spin arrangements at a temperature above T_C but below T_N, (b) the associated spin arrangements with respect to the points indicated on the M-H loop.

As stated above, there is a direct interface between the FM/AFM layer considered in the model depicted in Figure 1.7 and the temperature (T) of the system should be below the Néel temperature (T_N) of the AFM layer. The SG model also demands that the Curie temperature (T_C) of the FM layer is higher than the Néel temperature of the AFM layer. As can be seen from

Figure 1.7(a), without an external magnetic field, the spins of the AFM layers are arranged randomly (case 1) and the M-H loop of the system is centered around the zero axes. After applying the field cooling procedure, the system temperature is fixed to a certain value below T_N and a sufficient amount of external magnetic field is applied to saturate the ferromagnetic layer. Figure 1.7(b) illustrates various states of the spin arrangement at different points of the M-H loop. At the saturated point, the spins of the first AFM layer are aligned in a parallel direction (case 2) due to the exchange interaction at the interface. The spins in the next layer of AFM are then aligned antiparallel to maintain the antiferromagnetism. Both the FM and the AFM remain in a single domain state and it will continue even the magnetization is reversed. The spins of AFM are uncompensated and because of it, the coercivity and magnetization value of the system will be increased. Once the magnetization reversal has been started, the FM spins will try to align in the opposite direction (case 3). But since it is pinned by the AFM layer, it will need a larger force and higher external field to get this accomplished. As a result, the coercivity of the system will become even higher than in the previous case. On the other hand, when the magnetization field is reversed from the negative (case 4) to a positive value, the FM layer will not require the same amount of external field to actuate a torque. Rather, the external field for this case (case 5) will be lower as a torque is acting over the FM layer from all angles except the stable field cooling direction. Because of this energetically favorable case, the magnetization curve will shift to the negative values of the applied field which is termed as the exchange bias of the system. From this ideal model, it can be concluded that there are a couple of variables that control the exchange bias and coercivity. Some important variables are the temperature, nature, and thickness of the interfaces, the sequence of building blocks, size and shape of the final nanomaterial and training effect. Since MHNCs have different building blocks with different

sizes and therefore different interface types with different thicknesses, the exchange bias of the MHNCs can be very much unpredictable. One of the main objectives of our present study on NiO based MHNCs will be the investigation of the exchange bias, coercivity and other magnetization data with respect to the physical parameters.

The synthesis of MHNCs can vary based on the final structure and properties expected from the structure. There are several synthesis techniques for successfully growing 1D, 2D and 3D type heterostructures, including electrospinning, wet chemical method, sol-gel technique, microwave-assisted deposition or thermal decomposition, chemical vapor deposition and spray pyrolysis [7], [46]. Some of the wet chemical methods include one or two-stage hydrothermal methods or solvothermal, coprecipitation, and solution combustion methods. Hydrothermal methods are comparatively cheaper, environmentally friendly, easier to control and can be associated with other processes like microwave, electrochemistry, optical radiation and many more. This method involves the growth of the nanomaterials in aqueous solutions and water at ambient conditions such as low temperatures. Because of the water as the solvent, it is easier to control the growth of nanocrystals by controlling the temperature and pressure. The nanocrystals synthesized in our lab involved a two-step process. The first step is the thermal decomposition and the second step is the hydrothermal process. The details of the steps are explained in Chapter 2. Figure 1.8 depicts the steps involved in the synthesis process. Eight different MHNCs were produced (labeled as B1-B8) from nearly identical batches of NiO nanoparticles whereby all the parameters were held constant except the pH value of the reacting medium.

Two types of reactions may occur to the ions and the NiO precursor nanoparticles present in the hydrothermal solution due to water-based products depending on the pH of the solution – protonation and deprotonation. This happens because of the adsorption-desorption processes

occurring on the metal oxide (i.e., NiO) surfaces. Protonation refers to proton addition or deprotonation refers to the removal of a proton from the surface or an ion. In reality, the ionic form in aqueous solutions is better described as an ion complex having H_2O, OH^-, etc., ligands. During the protonation and deprotonation reaction, the mass, charge and chemical properties of the elements can change. Nanoparticles are prone to protonation and deprotonation in aqueous solutions. As an example, transition metal oxide (in this case NiO) nanoparticles react readily

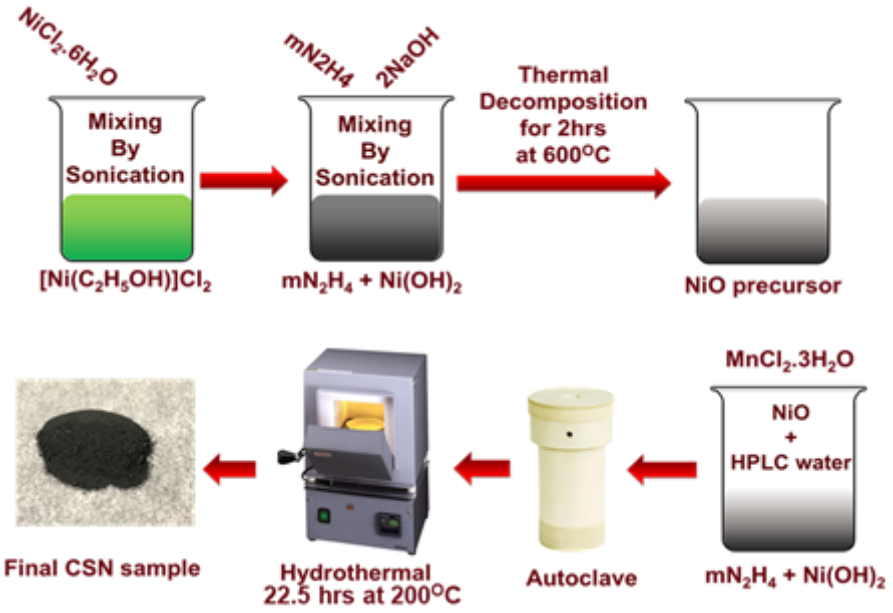

Figure 1.8: An illustration showing the complete synthesis process of the NiO based Magnetic Heterostructured Nanocrystals (MHNCs)

with the OH^- ion forming the surface-bound $>NiOH^-$ ions (the > symbol here represents Ni-O bonds at the surface of the NiO nanoparticle). Depending on the pH of the solution, $>NiOH^-$ can be further protonated or deprotonated. If the solution is acidic (low pH), $>NiOH^-$ will be protonated and if the solution is basic (high pH), deprotonation will be predominant. If there are other metallic ions present in the aqueous solution (Mn^{2+} or Mn^{3+}), they will tend to diffuse

through the layers (i.e. bound sheaths) of water molecules surrounding the nanoparticle by adsorption process to form an inner or outer-sphere complex. Figure 1.9(a) explains the process of the adsorption of metallic ions over a nanoparticle. As the adsorption of metallic ions changes due to pH, the shape of the final structure, thickness, and type of the adsorption material can change with the pH also. Hence, pH becomes a contributing factor in controlling the morphology as well as the physical properties of the grown nanocrystal. Figure 1.9(b) illustrates the effect of pH on the metallic ions present in aqueous solution.

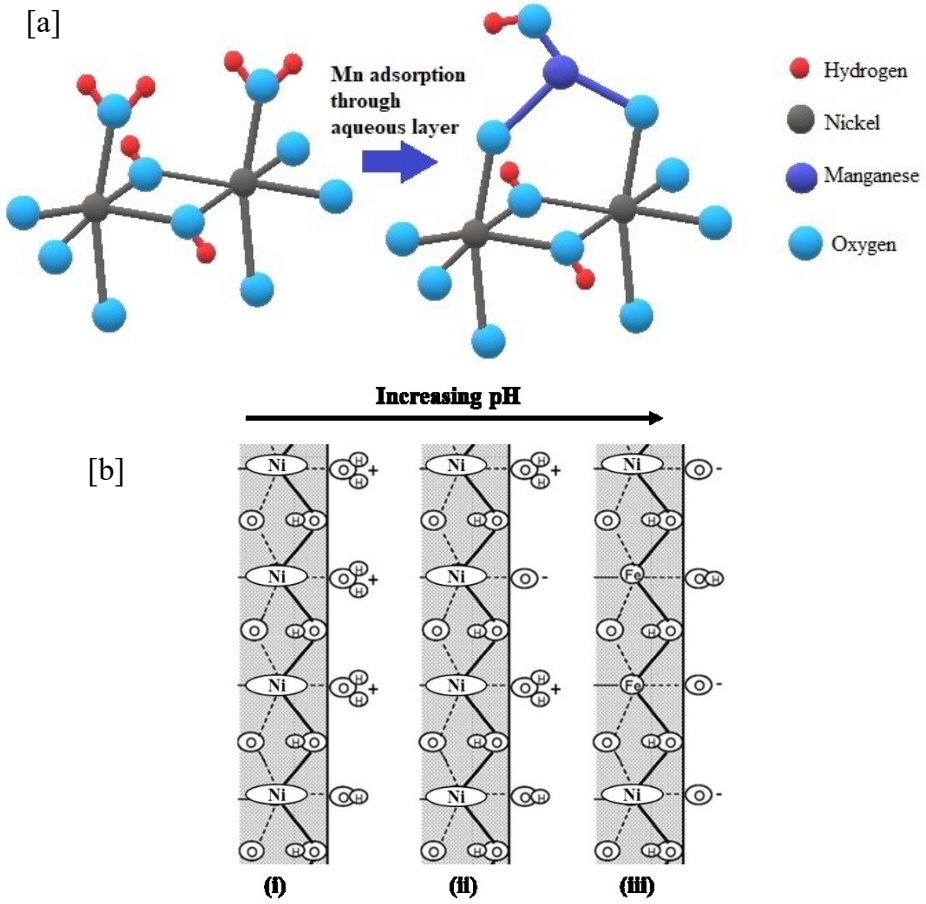

Figure 1.9: (a) An illustration depicting metallic ion adsorption in aqueous solution. (b) An illustration showing the effect of pH on the metallic ions present in an aqueous solution: (i) at low pH the surface is positively charged, (ii) at medium pH the surface is neutral, (iii) at higher pH the surface is negatively charged,

Previous studies in our lab showed that the NiO based core-shell nanoparticles (CSNPs) exhibit excellent coercivity or exchange bias [47][48]. However, it is not clear how the morphology is dependent on the process parameter such as pH of the synthesis medium. It is also unclear how the coating layer deposits over the NiO nanoparticles as a shell or nanoislands or both with respect to different pH. I hypothesize that the pH can change the shape, size, and thickness of the coating layer and because of that, the interaction between the interfaces can affect the exchange bias and coercivity. The purpose of this study is to understand how the heterostructured nanocrystals grow depending on the pH value of the solution medium during synthesis. Also, this study aims to understand the effect of the pH on the morphological, structural and magnetic properties of the grown heterostructured nanocrystals. In Chapter 2, the magnetic properties of the MHNCs, more specifically the changes in the coercivity, exchange bias, magnetic anisotropic energy, remanent magnetization and various ordering temperatures (blocking temperature, transition temperature etc.) with respect to different synthesis pH values, will be discussed. In Chapter 3, the focus will be on the morphological and compositional change of the MHNCs at various pH level by analysis of the XRD, TEM and XPS data.

CHAPTER 2: THE MAGNETIC PROPERTIES OF BIMAGNETIC HETEROSTRUCTURED NANOCRYSTALS HAVING A NiO CORE WITH $MN_XNI_{1-X}O$ SHELL AND/OR MN_3O_4 ISLANDS AND SYNTHESIZED UNDER VARYING pH CONDITIONS

Abstract

Bimagnetic heterostructured nanocrystals having an antiferromagnetic NiO core with a ferrimagnetic $Mn_xNi_{1-x}O$ shell and/or ferrimagnetic Mn_3O_4 islands have been synthesized in our lab under varying aqueous solution pH conditions. The two-step synthesis process first involves the growth of NiO nanoparticles, followed by the growth of the $Mn_xNi_{1-x}O$ and/or Mn_3O_4 nanophase over the NiO core using our hydrothermal method. The hydrothermal process involves protonation and deprotonation reactions occurring at the nanoparticle surface that vary in extent depending upon the pH, which may in turn directly affect the nature of deposition of the Mn-bearing nanophase on the surface of the NiO core. Our XRD analysis of a series of the heterostructured nanocrystals synthesized at pH values ranging from 2.4 – 7, suggests that there is a significant change in crystallite size with the adsorption and doping of Mn in terms of Mn_3O_4 islands and $Mn_xNi_{1-x}O$ coating. The magnetic properties, particularly the magnetic coercivity and exchange bias, are found to vary systematically with the pH of the synthesis conditions used to prepare the heterostructured nanocrystals. The magnetization measured as a function of temperature, in addition to the hysteresis loop data, support formation of $NiO/Mn_xNi_{1-x}O$ core-shell structures at the lowest pH, mixed $NiO/Mn_xNi_{1-x}O$ core-shell and NiO/Mn_3O_4 core-island structures for $2.4 < pH < 4.5$, and predominantly NiO/Mn_3O_4 core-island structures for $pH > 4.5$.

Introduction

Bimagnetic multi-component nanoparticles, either in core-shell, decorated or more complex topology and having antiferromagnetic and ferro/ferrimagnetic components, have been the subject of intense investigation due to their tunable magnetic properties. These magnetic heterostructured nanocrystals (MHNCs) have the potential for use in modern-day spintronic devices, magnetic random access memory (MRAM) devices, drug delivery, ferrofluids, pigments, and hyperthermia [1][2][3][4]. The MHNCs are also used in MRI contrast agents in place of conventional gadolinium-based contrast agents, GMR read heads in large capacity hard disk drives whereas their optical properties have been exploited for diagnostic purposes and making organic dyes [5]. Multiple benefits of antiferromagnetic based MHNCs such as nonvolatile memories, increased data processing speed, size miniaturization, and decreased power consumption have made them particularly suitable for spintronic devices [6][7][8]. Transition metal oxides, such as CoO, Cr_2O_3, MnO, and NiO, have been widely used as the antiferromagnetic component because they enable the tunability of the magnetic properties of MHNCs, including the fast switching times between spin states, weak interparticle relations and in overcoming the superparamagnetic limit [9][10].

NiO is antiferromagnetic (AFM) at room temperature having a rocksalt structure. The use of an AFM component in MHNCs is particularly advantageous because it enables the tunability of their magnetic properties. The exchange bias effect is vital for enabling the manipulation of the magnetic properties of MHNCs. The interface exchange coupling that drives the exchange bias of AFM/FM or AFM/FiM heterostructured nanocrystal systems can be manipulated to control the magnetic coercivity, spin-state switching times, and superparamagnetic blocking temperature. High magnetic anisotropy energy is inherent in systems with sizable magnetic

properties. The FiM layer spins are pinned towards the direction of the AFM layer raising the magnetic anisotropy of the system through interface exchange coupling [3][11][12]. Since magnetic anisotropy is highly dependent on the crystalline structure, shape, interface quality and composition [13][14][15], pH of aqueous solutions in hydrothermal synthesis can be an important factor for achieving high magnetic anisotropic energy. For example, for small and faceted nanostructures, the magnetic anisotropic energy can be high as there are more spin clusters than spherical and big nanoparticles [14].

Initial work in our laboratory has demonstrated that significant coercivity and exchange bias fields are obtainable for NiO-$Mn_xNi_{1-x}O$-Mn_3O_4 MHNCs at low temperatures (5K) and reasonable values are possible at room temperature [16]. However, it is not clear from this work how the coercivity and exchange bias is controlled by the size and morphology of the nanoparticles and by the pH of the aqueous solution used in the hydrothermal synthesis portion of sample preparation. Proton binding on the surface of metallic oxide nanoparticles (NP) in aqueous solutions, which is also referred to as protonation, is controlled in large measure by the solution pH [17][18]. The OH^- ion in the aqueous solutions are very reactive in presence of an oxide nanoparticle and react with the metallic part of the NPs via hydroxylation reaction forming >MOH units, where M is the metallic ion and (>) represents the bonds to the lower atomic layer [19][20]. For NiO nanoparticles, the >NiOH unit that forms by hydroxylation reaction gets protonated ($>NiOH+H^+ \rightarrow >NiOH_2^+$) or deprotonated ($>NiOH \rightarrow >NiO^- + H^+$) depending on the pH of the aqueous medium. On the other hand, aqueous metal ions or cations (in this case Mn^{2+}) diffuse through layers of water molecules surrounding an NP and undergo reactions to form either an inner-sphere complex via chemical bond ($>NiOH + Mn^{2+} \rightarrow >NiMnO + H^+$), outer-sphere complex via ion pair ($>NiOH + Mn^{2+} \rightarrow >NiO^-–Mn^{2+} + H^+$), or be in the diffuse swarm

of the double-layer [20]. As the Mn^{2+} ion has to compete with H^{+} ions present in the solution, solution pH becomes a determining factor for the adsorption of Mn^{2+} ions over the NP surface. If the pH of the solution is higher, deprotonation of the metallic oxide will be higher resulting in more sites available for the adsorption of Mn^{2+} ions, hence larger coating thickness. In lieu of our general understanding of these principles, the effect of pH on the size and shape of nanoparticles in hydrothermal synthesis has been successfully interpreted by others [21][22][23][24]. Our objective in this work is to understand how the pH is affecting the adsorption during hydrothermal synthesis and how the pH is changing the morphology as well as the magnetic properties of the MHNCs. The synthesis procedures used to prepare a series of NiO nanoparticle coated with a $Mn_xNi_{1-x}O$ shell and Mn_3O_4 decorated islands at pH values ranging from 2.4 – 7 are presented here. Besides, we discuss the characterization of the structural, morphological and magnetic properties of our NiO- $Mn_xNi_{1-x}O$- Mn_3O_4 MHNCs.

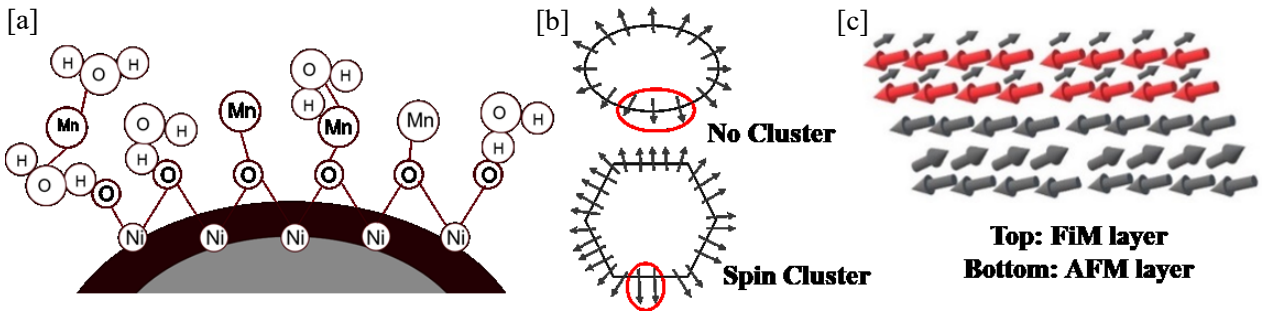

Figure 2.1: (a) Adsorption of Mn^{2+} ions over NiO core in aqueous solution (b) Pseudo-spherical nanostructure with no spin cluster (top) and faceted nanostructure with spin cluster (bottom), and (c) Spin-spin interaction at the interface of an AFM-FiM layer.

Experimental Methods

The MHNCs were synthesized using a two-step process. The first step follows the procedure described by El Kemary et. al. [25] and involves the thermal decomposition of

$Ni(OH)_2$ to produce the NiO precursor. First, 0.11 M of $NiCl_2.6H_2O$ was dissolved in absolute ethanol and then added to NaOH and $N_2H_4.H_2O$ to that solution. The ratio between $NiCl_2.6H_2O$, $N_2H_4.H_2O$, and NaOH was maintained at 1:5:10. The solution was then stirred using a magnetic stirrer and put in an oven under an open atmosphere for 2 hours at 600°C to dry and activate thermal decomposition. The resulting powder containing NiO was washed with deionized (DI) water and then centrifuged to get rid of excess water and residue.

Next, our hydrothermal nanophase epitaxy process described previously [8][26][27] was used to grow the Mn-bearing oxide phases over the NiO core. First, $MnCl_2.3H_2O$ was added to deionized water after the water was purged with N_2 for 15-20 minutes at a temperature of 70-80°C. The pH of the solution was adjusted by adding drops of HCl or NaOH. Next, 0.33g of NiO nanoparticles were added to a 0.5 M $MnCl_2.3H_2O$ aqueous solution. After adding NiO nanoparticles to the $MnCl_2$ solution, the mixture was stirred for 25-30 minutes and then placed in an autoclave. The autoclave was kept in a furnace for 22.5 hrs at a temperature of 200°C for hydrothermal treatment. Once the hydrothermal synthesis was complete, the product was rinsed using DI water, centrifuged and then dried at a temperature of ~50°C. Table 2.1 lists the samples that were prepared using the methodology described above, at various pH values of the solution.

XRD analysis of all the samples was made using a Bruker D8 Discover diffractometer using Cu Kα X-ray source with a wavelength of $\lambda = 1.54184$Å. The diffractometer was operated at 40kV and 40mA with a 0.6mm slit on the incident x-ray beam. All XRD patterns were refined using TOPAS software via the Rietveld method. The SEM analysis was made using an FEI-Quanta 200 instrument operated at 20kV. The samples were prepared by first carbon coating and then placing them on copper tape for SEM analysis. TEM samples were made via probe sonication machine in aqueous solution using hexane. After sonication, the samples were dried

for 1-2 minutes and dispersed on a Lacey 300 Cu grid. Magnetic data were measured using a Quantum Design Physical Property Measurement System (PPMS). For the magnetization vs temperature data, both field-cooled (FC) and zero-field-cooled (ZFC) measurements, the samples were first cooled to 5 K from room temperature, in a field of 100 Oe for the FC curve, and the magnetization data was collected in a 100 Oe external field. Both the FC and ZFC hysteresis curves were measured from -18000 Oe to 18000 Oe at different intervals and at 5 K. The sample was cooled in a field of 100 Oe for the FC M vs H hysteresis measurements.

Table 2.1: List of samples synthesized at various solution pH

Sample	B1	B2	B3	B4	B5	B6	B7	B8
pH	2.39	2.98	3.52	4.02	4.48	5.03	6.02	7.03
size (nm)	29.34	29.69	28.74	29.24	25.03	27.74	25.53	24.89

Results and Discussion

In Figure 2.2 we show the XRD patterns collected from the samples of this study. Rietveld refinement of the patterns shows the presence of three distinct phases in the samples: NiO, $Mn_xNi_{1-x}O$, and Mn_3O_4, which is fully consistent with our initial study on this system [16]. Both the NiO and $Mn_xNi_{1-x}O$ phase have a rocksalt structure ($Fm\bar{3}m$) whereas Mn_3O_4 has a spinel structure with the space group I41/amd [28][29][30].

Figure 2.2(a) shows different XRD patterns of the MHNCs samples including one of the NiO nanoparticle samples before hydrothermal synthesis. Since NiO and $Mn_xNi_{1-x}O$ share the same structure and space group, their peaks are overlapped with NiO but there is also a slight shift. This shift is attributed to the difference in the ionic radii of Ni^{2+} (0.69 Å) and Mn^{2+} (0.80 Å) [31] thus affecting the lattice parameter of the rock salt crystal structure of $Mn_xNi_{1-x}O$ (a =

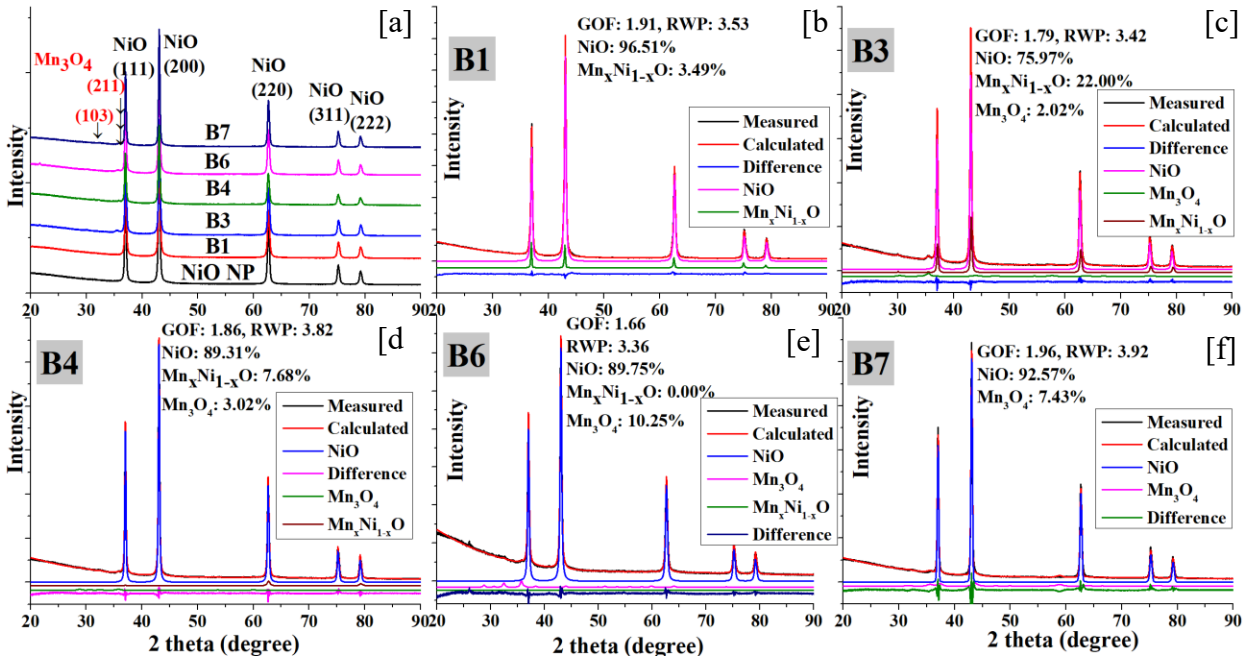

Figure 2.2: (a) Fitting and Rietveld refinement of the sample B1, B3, B4, B6, and B7;(b-f) Sample B1 has no Mn_3O_4 peaks, B3 and B4 has both Mn_3O_4 nanoisland and $Mn_xNi_{1-x}O$ shell peaks; B6 and B7 does not show any peak for $Mn_xNi_{1-x}O$ shell.

4.44 Å for MnO, a ≈ 4.350-4.210 Å for 25-75% Mn doping) with that of NiO (a = 4.17 Å) [32]–[34]. The largest peak of the I41/amd Mn_3O_4 structure, (211) at 2θ ≈ 36.2 is visible in all of the MHNCs XRD spectra [Figure 2.2(a)]. Mn_3O_4 has tetrahedral sites that exchange cations (Mn^{2+}, and Mn^{3+}) with NiO, and $Mn_xNi_{1-x}O$ from their octahedral sites for rearrangement, where there is the formation of a rocksalt-spinel joined nano-structure, which will be further elucidated below [35][36]. As shown in the XRD spectra, sample B1 has little contribution (3.49%) from $Mn_xNi_{1-x}O$ shell regions which increased significantly for sample B3 (22.00%) and at a fair amount for sample B4 (7.68%). Other than the $Mn_xNi_{1-x}O$ shell there is also the Mn_3O_4 phase present in both B3 and B4 spectra which continues to increase up to sample B6 and then drops again at sample B7. Surprisingly the $Mn_xNi_{1-x}O$ shell contribution in sample B6 is zero and that continues for sample B7 also. It can be summarized that the lower pH allows more $Mn_xNi_{1-x}O$ shells while the

upper pH allows more Mn_3O_4 phases. The associated goodness-of-fit (GOF) and Rwp values given in the respective figures affirm the fitting of the peaks. We have used the Scherrer formula $D = k\lambda/\beta\cos\theta$ [37] to measure the crystallite size of the samples from the XRD data. Table 2.1 shows the nanocrystallite size of sample B1 to B8: the size of the NiO nanoparticles prior to hydrothermal synthesis is 23.57 nm as determined using the Scherrer formula.

In Figure 2.3 we show the TEM images and elemental maps taken from sample different MHNCs samples. Figure 3(a-d) are low-resolution TEM images depicting the shape of the nanoparticles. The majority of the particles seem to be faceted structures whereas some area show pseudo-spherical shaped particles. The results are in good comparison with previous studies [8][16] which also showed the same type of morphology for core-shell nanoparticles. Figure 2.3(a) shows a core-shell type form of sample B1 with no Mn_3O_4 islands in it while sample B3 in Figure 2.3(b) shows the presence of both shell and nanoislands. Figure 2.3(c) shows a TEM EDS mapping of sample B6 confirming the presence of Mn in both shell and island. Decorated nanoisalnds grown on top of the sample are also seen in sample B6 TEM EDS image. But there is no shell region visible in sample B7 shown in another EDS mapping [Figure 2.3(d)]. Although there is no visible peak of the $Mn_xNi_{1-x}O$ shell region in XRD data for sample B6, we can see a little bit of shell in the TEM image. But the absence of a shell in sample B7 matches with the data found from XRD spectrum also.

High-resolution TEM analysis in Figure 2.3(f) reveals the presence of Mn_3O_4 islands and $Mn_xNi_{1-x}O$ shell regions grown on the NiO core. The structure reorients to accommodate the cations among each other and the preferred direction for this reorientation is found as [111]. The directions of the planes are found from the FFT image analyzed by Crystbox software [38]. It has been established that during the growth of the Mn_3O_4 nanophases on MnO, four octahedral

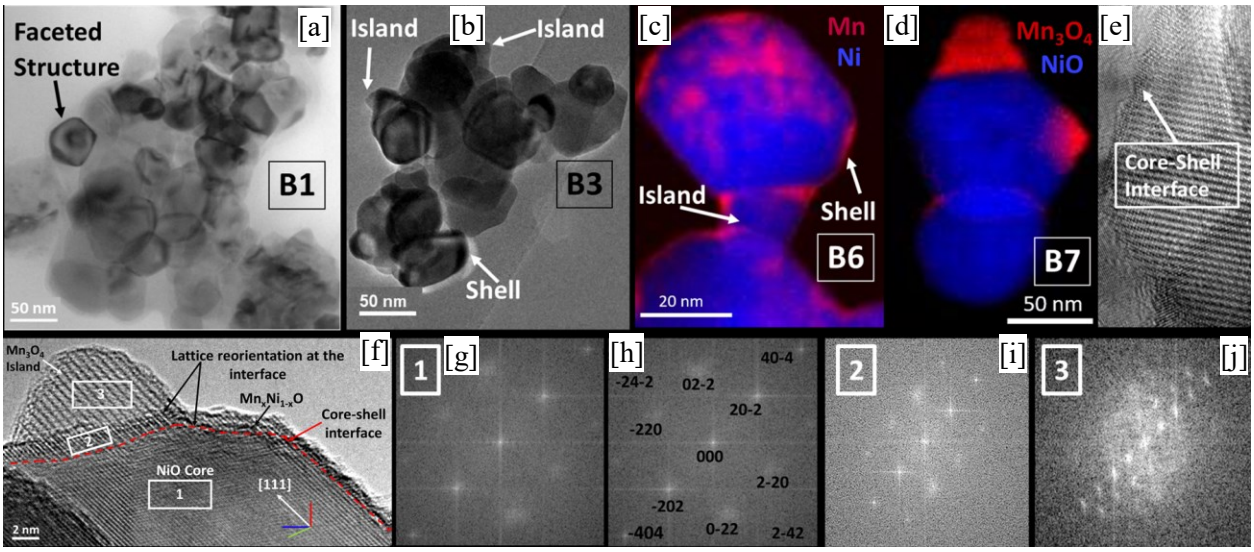

Figure 2.3: (a) TEM images of sample B1 showing the faceted structure and shell, (b) sample B3 showing both shell and islands, (c) TEM EDS showing Mn in both shell and islands of sample B6, (d) sample B7 showing no shell but Mn_3O_4 islands; (e) High-resolution TEM image showing core-shell interface and lattice mismatch, (f) HRTEM image shows the core, shell, nanoislands and the interface between them, (g,h) FFT images of NiO core and respective planes: (i) $Mn_xNi_{1-x}O$ shell FFT and (j) Mn_3O_4 islands FFT

cation vacancies surrounding a tetrahedral Mn^{3+} should be observed at the MnO-Mn_3O_4 interface region [36]. These misalignments and vacancies are visible in Figure 2.3(e) and 2.3(f) at the core-shell interface. The reason behind this can be attributed to the fact that the structure becomes relaxed once the vacancies are created giving every Mn^{3+} cation impetus to reorient and take the position. Also as the ionic radius of Mn^{3+} are smaller than Mn^{2+} and the ionic radius of Mn^{2+} is higher than Ni^{2+}, there are some misalignments during the growth of the coating layer. These misalignments are also noticeable along the red dotted line in Figure 3(f). This is also seen from the Fast Fourier Transforms [FFT] of the NiO, $Mn_xNi_{1-x}O$ and Mn_3O_4 regions shown in Figure 2.3(g), 2.3(i) and 2.3(j) respectively. The FFT image of Mn_3O_4 has more planes and plane alignments than for either $Mn_xNi_{1-x}O$ or NiO regions. This confirms the structural change and misalignments from the rocksalt to the spinel structure.

The temperature dependence of the FC and ZFC magnetization (M) curves measured as a function of temperature (T) of samples B1 to B8 are presented in Figure 2.4. The ZFC curves increase from an initial negative magnetization value, reach a peak (or show two peaks) and then decrease and generally approach the FC curves at temperatures above ~200 K. There is an absence of the bifurcation or irreversibility temperature, where the FC and ZFC curves split from each other, in the M-T curves measured from our samples at the applied field of 100 Oe. The absence of bifurcation temperature could be due to two reasons: (i) either it is higher than 300K, or, (ii) it may be due to the application of too high of the external field in the measurement of the M-T curves [39][40]. There are two peak-like features evident in the ZFC curves for samples B2 and B4 below ~110 K, which coincide respectively with sudden onsets of increasing FC magnetization with decreasing temperature. For samples B5 – B8, the peak occurring in the ZFC curves above 100 K is absent and only the lower temperature peak remains. The sudden onset of the increase in the magnetization in the FC curves, along with the corresponding drop-off in the ZFC curve, with decreasing temperature, is characteristic of a Curie transition behavior. The Curie temperature of the FiM Mn_3O_4 nanophase has been identified to occur at ~42K [36][41][42]. Thus, we identify the low-temperature peak like feature (T_{C1}), occurring between 62 to 89 K in the ZFC M-T curve with the freezing of the FiM spins in the Mn_3O_4 decorating islands. Our previous study established that the $Mn_xNi_{1-x}O$ nanophase of the $NiO/Mn_xNi_{1-x}O$ heterostructured nanoparticles has FiM properties [16]. Accordingly, we attribute the higher temperature transition (T_{C2}), occurring in the 103 to 108 K range in the ZFC M-T curve, with the freezing of the FiM spins in the $Mn_xNi_{1-x}O$ shell layer on the MHNCs. The T_{C1} and T_{C2} values are tabulated for our samples in Table 2.2. Based on this interpretation, samples B2 – B4 possess both the $Mn_xNi_{1-x}O$ shell layer and the decorating Mn_3O_4 islands whereas samples B5 – B8 have

predominantly Mn_3O_4 islands decorating the NiO nanoparticles. The ZFC M-T curve for sample B1 does not exhibit a peak below 100 K: We attribute this to the lack of deposition of the Mn_3O_4 nanophase on the MHNCs for the lowest solution pH value (2.39).

Since our nanoparticles were tightly packed for M-T measurements, meaning that interparticle dipolar interactions are present, and have a finite size distribution, we use the -d(FC – ZFC)/dT plotted vs temperature (note: FC was measured in the warming mode and is thus consistent with this definition) to determine the mean blocking temperature ($\langle T_B \rangle$, which we simply refer to as T_B) for a measurement field of 100 Oe [43]. Some of the additional effects which warrant the use of the aforementioned definition for T_B include the presence of uncompensated spins, AFM vs FiM crystalline anisotropy, spin clusters, and lattice strain particularly at the interface between the core and $Mn_xNi_{1-x}O$ shell and between core and decorating Mn_3O_4 islands. We show the plots of -d(FC – ZFC)/dT vs T, which are used to determine the T_B values (for samples B1, B3, B5 and B7) in the later part of this section. Table 2.2 shows the T_B values determined for samples B1 to B8. The greater blocking temperature (≥ 90 K) for samples B1 – B4 is assigned to the $Mn_xNi_{1-x}O$ shell whereas the lower blocking temperatures (~ 46 K) are assigned to the decorative Mn_3O_4 islands. The fact that the Néel temperature for AFM NiO nanoparticles having a diameter of 20-60 nm exceeds 350 K [44] is consistent with the lack of a blocking temperature being attributed to the magnetically soft AFM phase in our bimagnetic nanoparticles. We note that ZFC M-T curves decrease and eventually become negative below T_{C2} for samples B1 – B4 or below T_{C1} for samples B5 – B8, whereas the FC curves generally increase in this range. This effect, which was predicted by Néel and verified for magnetic materials having two or more sublattices with FiM ordering [45], occurs due to one sublattice of the FiM shell/island nanophase progressively overcoming the contribution due to

the other FiM sublattice as the temperature is lowered, in the ZFC case. It is not known how additional effects due to surface and interface anisotropies, lattice strain, and spin clusters may contribute to the FiM sublattice and overall M-T behavior.

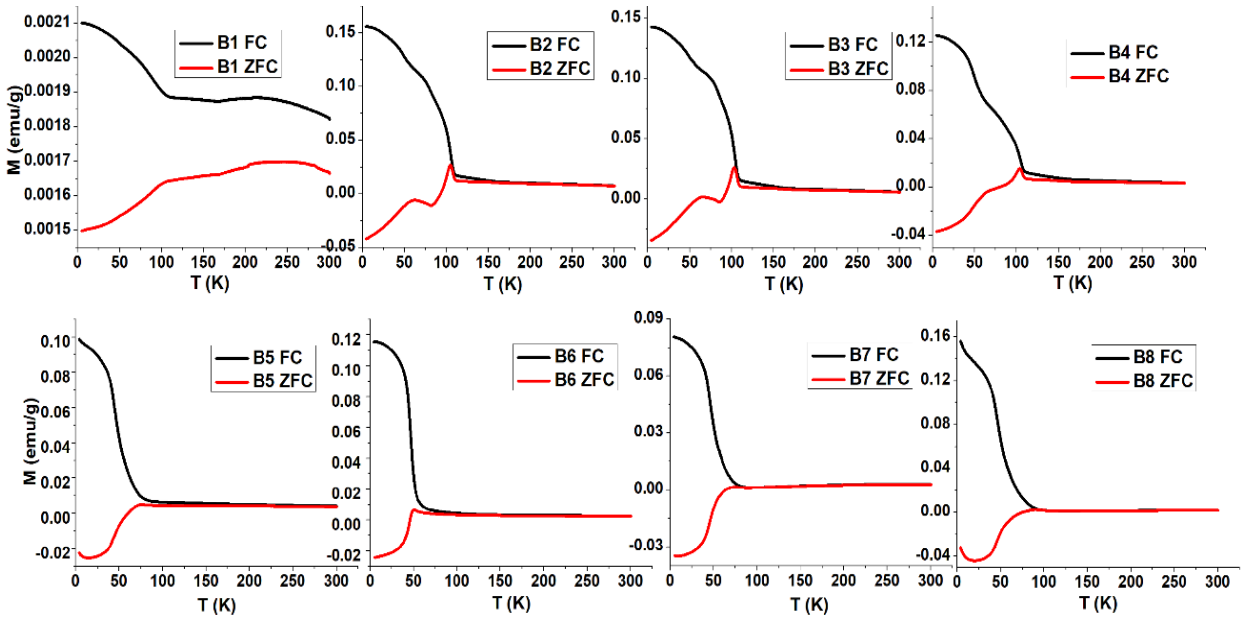

Figure 2.4: Magnetization vs temperature curves at field-cooled and zero-field-cooled conditions for sample B1 to B8.

Table 2.2: Blocking and bifurcation temperature of different samples

Sample		B1	B2	B3	B4	B5	B6	B7	B8
Transition Temp. (K)	T_{C1}	--	62	63	65	74	50	74	89
	T_{C2}	108	105	103	104	--	--	--	--
Blocking Temp. (K)	T_B	90	103	100	102	45	46	45	46

Low temperature (5K) magnetization, M vs magnetic field, H hysteresis data (M-H loops), for both the FC and ZFC conditions, are presented in Figure 2.5. The coercivity (H_C), remanent magnetization (M_R), saturation magnetization (M_S) and exchange bias field (H_E) values

derived from the hysteresis data for the samples of this study are shown in Table 2.3. The exchange bias values were calculated using the coercivity value for ZFC and FC values and the following formula: $H_E = | H_{C+} - H_{C-} |/2$. The saturation magnetization was determined by extrapolating values from the M vs 1/H graph. Figure 2.5 indicates that the low-temperature M-H loops change significantly with increasing pH values from sample B1 to B8. The hysteresis loops exhibit the standard letter "S" shape for samples B1 – B4 and oval-tilted-like appearance for samples B5 – B8. The hysteresis loops for samples B5 – B8 has more of a linear trend with particularly large coercivities for samples B6 and B7. Our M-T results are consistent with B6 having the highest coercivity and exchange bias and B8 having the highest saturation magnetization value.

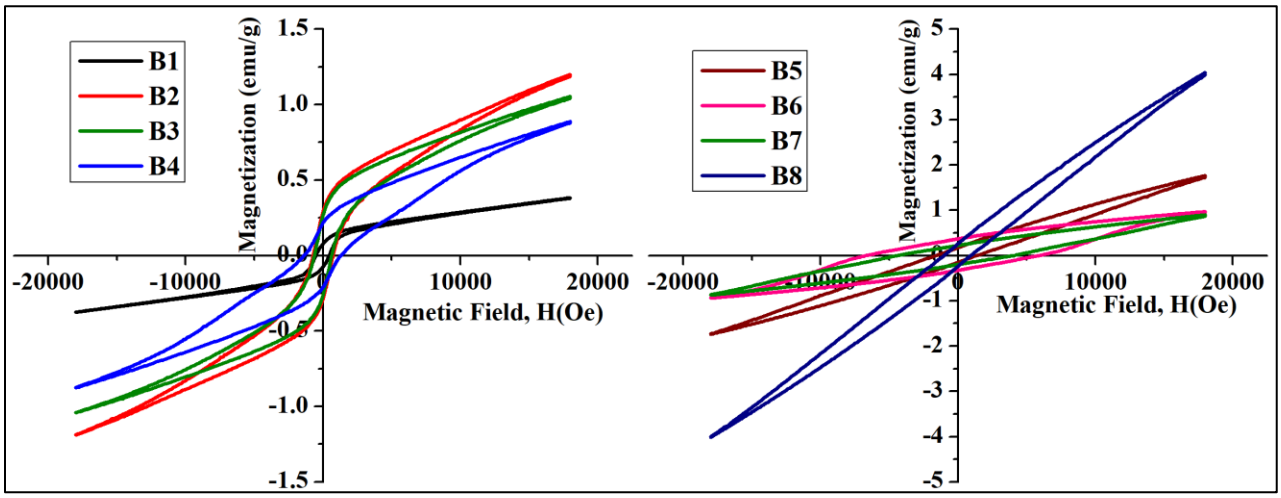

Figure 2.5: Magnetization (M) vs magnetic field (H) curves for sample B1 to B8

As was alluded to above, both the $Mn_xNi_{1-x}O$ and Mn_3O_4 nanophases covering the NiO core of our MHNCs have FiM properties. Thus, the trend exhibited by the shape of the hysteresis loops in Figure 2.5 can be explained by domain-size effects attributed to the $Mn_xNi_{1-x}O$ and Mn_3O_4 FiM nanophases, where the mean size of the domain appears to be controlled by the value

of pH used during the synthesis of our MHNCs. At lower pH values up to ~4, the M-H loops show similar "S" shape characteristics, indicating the existence of multiple domains, whereas with increasing pH (from ~ 4 to ~7) the overall linear-oval shape is consistent with the predominance of single domain FiM nanophases [46][47]. It needs to be emphasized that the change of overall domain size is gradual from sample B1 to B8 with multiple sized domains being present in between. For example, the hysteresis loop measured from sample B4 in Figure 2.6(b) can be attributed to pseudo-single FiM domains in the specimen. The hysteresis data measured from the pseudo-single domain FiM phase typically has a mixture of single-domain (SD) attributes, namely high remanence, and multiple-domain (MD) features, particularly low coercivity [46]. Sample B6 has the highest coercivity (~ 5.9 kOe; see Table 2.3) indicating that this MHNC specimen has the largest SD domain structure, which is consistent with the B6 having the largest FiM nanophase grain size. Samples B7 and B8 still maintain an SD FiM structure but their hysteresis data are consistent with these specimens having smaller FiM grain sizes [46][48]. For the same reasons outlined just above, the remanent magnetization is also the largest for sample B6 within the sample B5 to B8 group (see Table 2.3). The shape of the hysteresis loop of sample B1 (pH 2.39) is consistent with the MHNCs having a relatively large AFM core and considerably smaller-sized shell regions [49]. The lowest values of coercivity, exchange bias and remanent magnetization for sample B1 among the set of samples are consistent with this. Furthermore, the trend exhibited in Table 2.3, particularly for the coercivity and the exchange bias, indicates that as the pH value of the initial aqueous solution is lowered, the adsorption of Mn^{2+} ions is hindered and, hence, there is less deposition of the FiM nanophase ($Mn_xNi_{1-x}O$ and Mn_3O_4) onto the surfaces of NiO nanocrystals. Conversely, as the pH value is increased, greater deposition of the FiM nanophases is achieved until a value of ~ 4.5 (for sample

B5), at which point we obtain a predominance of the decorating Mn_3O_4 islands deposited on the NiO nanocrystals. Beyond this value in pH (~4.5), the deposition of the Mn_3O_4 nanophase is maximal, as gauged by grain size, for pH of ~5 and then declines with increasing pH beyond this value. This is confirmed in a plot of the coercivity and exchange bias vs pH, both of which are seen to peak for a pH value of ~5, as shown in Figure 2.7. As alluded to above, the reduction of the coercivity and exchange bias values for samples B7 and B8, relative to those of B6, as pH is increased beyond ~5 can be attributed to the overall reduction in size of the decorating Mn_3O_4 islands. The shape of the M-H loop and lower coercivity vs very high M_S values for sample B8 is strongly consistent with Mn_3O_4 as a highly predominant SD FiM nanophase component of the

Table 2.3: Magnetic data from M-H loop analysis

Sample	B1	B2	B3	B4	B5	B6	B7	B8
Saturation Magnetization, M_S (emu/g)	0.55	1.32	1.67	0.91	1.88	0.99	0.93	4.37
Remanent magnetization, M_R (emu/g)	0.08	0.29	0.26	0.22	0.18	0.37	0.22	0.26
Coercivity, H_C (Oe)	511.3	934.3	826.0	1530.0	2350.7	5860.4	4122.9	1011.5
Exchange Bias H_E, (Oe)	165.5	620.8	602.0	1670.9	2199.9	2952.5	1444.6	833.1
K_{eff} (J/m^3)	0.02 $x10^4$	--	--	--	0.33 $x10^4$	0.43 $x10^4$	0.29 $x10^4$	0.33 $x10^4$

MHNCs. We note that the nature of the nanophase, i.e., $Mn_xNi_{1-x}O$ vs Mn_3O_4, has a determinative factor on MD vs SD formation in relation to its physical grain size: The $Mn_xNi_{1-x}O$ phase appears to favor formation of MD whereas the Mn_3O_4 phase appears to favor SD formation for similar sized grains.

Because of the relatively well-ordered, generally epitaxial nature of the core-shell/island interface of our MHNCs, there is prominent AFM-FiM coupling and a strong pinning effect at the interface. This pinning effect plays a pivotal role in increasing the magnetocrystalline anisotropy and exchange bias in MHNCs [46][50]. Another important factor of increased pH is the surface anisotropy due to the shape of crystallites. From the TEM images, it is clear that the crystallites have a faceted and pseudo-spherical shape. The faceted structure has more surface anisotropy than pseudo-spherical or spherical structure because of broken symmetry, strain or defects [51][52][53]. Also, faceted nanocrystallites are expected to have more spin clusters than spherically shaped ones (Figure 2.1). As pH increases and adsorption changes, preferential growth of the FiM nanophase coating layer over faceted planes generally enhances surface and magnetocrystalline anisotropies. From the HRTEM analysis and XRD data, it is clear that there are misalignments at the interface of the structure along with vacancies. These misalignments and vacancies increase stress and surface anisotropies. All these factors contribute to the change of saturation and remanent magnetization from sample B1 to B8.

In this section, we examine the nature of the shift between the FC and ZFC hysteresis loops of our MHNCs in more detail. The FC hysteresis loops shown in Figure 2.6 are shifted along the negative H axis (H_E) orientation and along with the positive M axis orientation when compared to the ZFC curves, indicating strong exchange bias fields for our HMNC samples. Furthermore, whereas the H_E values are seen to change with pH value used to synthesize the

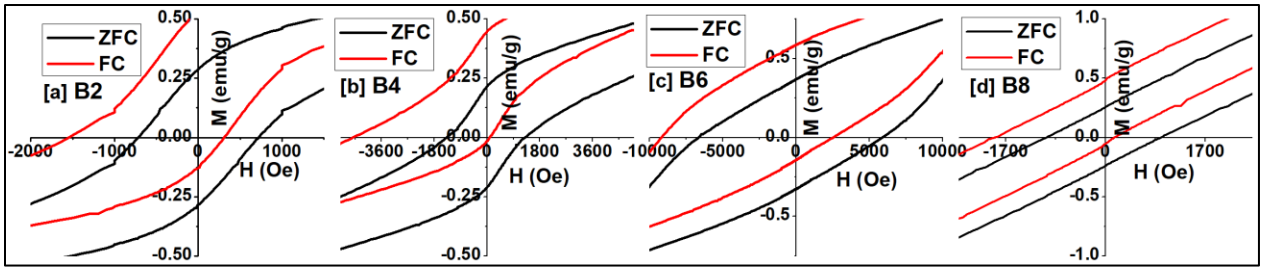

Figure 2.6: Exchange bias and magnetization vs magnetic field curves for 5K at filled cooled and zero filled cooled condition of (a) sample B2 (b) sample B4 (c) sample B6 and (d) sample B8.

samples as discussed above, the shift of the FC vs ZFC M-H loops along the M axis (i.e. vertical shift) is generally consistent for all samples. Zheng et al. [54] and He et al. [55] have attributed such vertical shifts in the FC M-H loops of Fe/Fe_2O_3 and Ni/NiO core-shell nanoparticles, respectively, to frozen spins at the surface of the AFM metal oxide layer. The larger M values result for the loop measured in the positive field direction because this coincides with the FC field orientation and the orientation of the frozen surface spins, which cannot be flipped when the H field is reversed in the opposite direction, resulting in lower M values. Similarly, we attribute the vertical shift of the FC M-H loops measured from our samples to the frozen Ni spins at the surface and/or interface of the NiO AFM core of our MHNCs. The nearly uniform vertical shift of the FC M-H loops is consistent with the uniformity in size and morphology of the NiO precursor nanoparticles used in the final-step synthesis of our B1 – B8 samples. Furthermore, the frozen, spin-glass like spins result from disorder effects at the surface and/or interface of the NiO core. The disorder effects were discussed above (i.e., misfit dislocations, vacancies, stacking faults, etc.) and are clearly seen in the HRTEM images in Figure 2.3. In addition, the frozen Ni spins in the NiO core and the Mn spins from the $Mn_xNi_{1-x}O$ shell layer or the Mn_3O_4 islands immediately at the interface between the AFM-FiM phases are largely uncompensated in the immediate vicinity of misfit dislocations, vacancies, stacking faults, and other defects [56]. Such

uncompensated interface spins are deemed to be critical for an exchange bias effect to be present in heterostructured nanocrystals. Our M-H loop data measured from our MHNCs are consistent with this view. The AFM anisotropy of NiO nanophases is known to be relatively small in comparison to that of FiM anisotropy of spinel nanophases [57]. Nevertheless, due to the sizable H_E values recorded for our samples, likely, the frozen AFM spins also participate in the exchange bias effect in our MHNCs. However, to our knowledge, whether the frozen uncompensated AFM spins at the interface are excluded from or included in participating in the exchange bias of MHNCs is as yet unclear.

In addition to the spin-spin interactions alluded to above, domain structure, morphology, and spin clustering are deemed to be important for the manifestation of the magnetic properties of MHNCs. Nanophase Mn_3O_4 has been purported to have a large overall anisotropy, which should have a strong bearing on the magnetic properties of bimagnetic nanoparticles [3]. In our MHNCs, Mn_3O_4 forms as islands over the core and, as shown in our TEM images, contributes to nominal roughness, lattice strain, and the formation of vacancies at the core-island interface. Also, as alluded to above, the formation of spin clusters is likely on the surface of the Mn_3O_4 islands. This is also generally the case for the $Mn_xNi_{1-x}O$ shell surrounding the NiO core, except that much fewer spin clusters are expected to form on the surface of this nanophase. The anisotropy of the $Mn_xNi_{1-x}O$ shell layer is expected to be smaller than that of the Mn_3O_4 islands because of the crystal structure. Mn_3O_4 is a spinel phase, which is known to have considerable anisotropy values, whereas the $Mn_xNi_{1-x}O$ shell is at best a disordered phase (the Mn spins are not arranged among a periodic magnetic lattice) and thus has a lower anisotropy. To estimate the effective anisotropy constant (K_{eff}) of the Mn-bearing nanophases, we assume weak particle-particle dipolar interactions and use the Kneller formula: $H_C = \frac{2K_{eff}}{M_S}(1 - (\frac{T}{T_B})^{1/2})$ [59][60].

Further assumptions in the use of Kneller's formula include single domain particles having uniaxial anisotropy. As a result, the estimated K_{eff} values should be treated with caution. Table 2.3 shows our estimates of K_{eff} for samples B1 and B5 – B8; the rest of the samples have both the $Mn_xNi_{1-x}O$ and Mn_3O_4 nanophase and their magnetic data cannot be used to provide unique, single FiM phase anisotropies. The estimated K_{eff} values for the Mn_3O_4 nanophase (samples B5 – B8) range from 0.29 – 0.43 x 10^4 J/m^3 and are seen to be considerably larger than for the $Mn_xNi_{1-x}O$ nanophase (sample B1), having a value of 0.02 x 10^4 J/m^3.

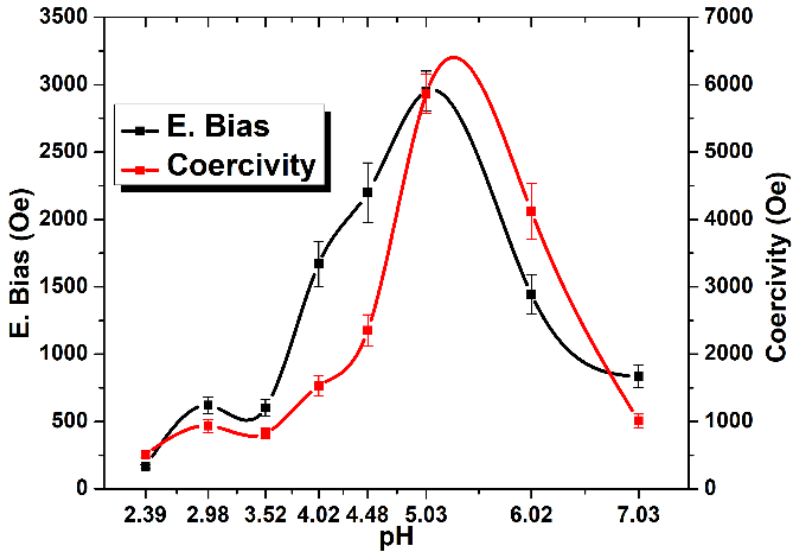

Figure 2.7: Coercivity and Exchange Bias of samples B1 to B8

Figure 2.8 represents the susceptibility vs magnetic field (H) data of a few of the samples where susceptibility was taken as a derivative of M data vs H. According to Nerio et. al. the maxima of these graphs (arrowhead) characterize the magnetization reversal of the phases present in the structure [49]. Besides, magnetization reversals are purported to be a good indicator of the exchange bias effect in magnetic heterostructures [61][62]. The susceptibility data for samples B1 and B2 do not show prominent second maxima whereas the data for the

remainder of the samples have at least one additional set of maxima and for samples, B7 and B8, have also a set of third maxima. We conjecture that, for consistency with our discussion above, the principal maxima (centered at H = 0) coincide with NiO-core-$Mn_xNi_{1-x}O$-shell spin-spin interactions whereas the second maxima coincide with NiO-core-Mn_3O_4–island spin-spin interactions. This is consistent with the reduction of the first maxima, coinciding with the reduction of the $Mn_xNi_{1-x}O$ shell nanophase, and the general increase of the higher-order maxima, coinciding with the emerging predominance of the decorating Mn_3O_4 islands, with increasing pH used to synthesize samples B1 to B8. The third maxima in B7 and B8 may be a result of a distinct phase of Mn_3O_4 whereas the position of second maxima at a lower value than B6 indicating smaller exchange bias is in good agreement with previous data.

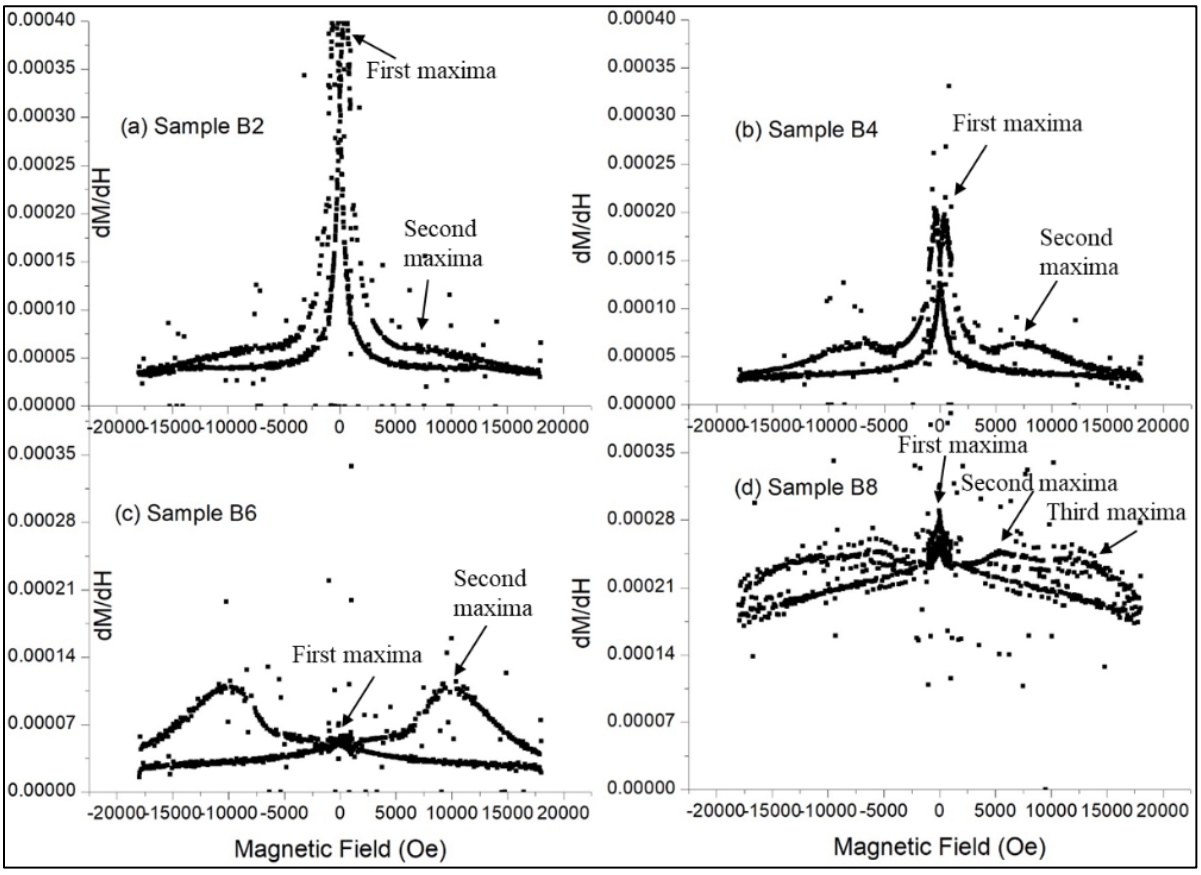

Figure 2.8: susceptibility vs magnetic field of (a) sample B2 (b) B4 (c) B6 and (d) B8

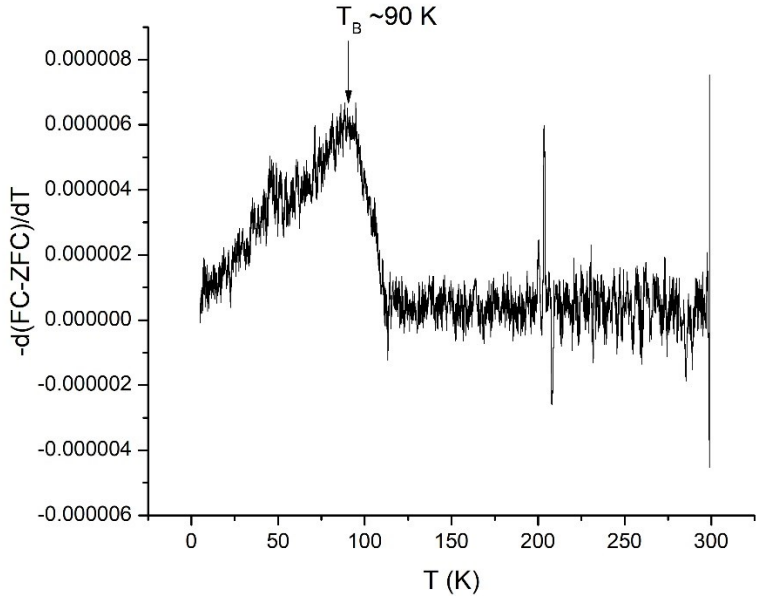

Figure 2.9: Blocking temperature of sample B1

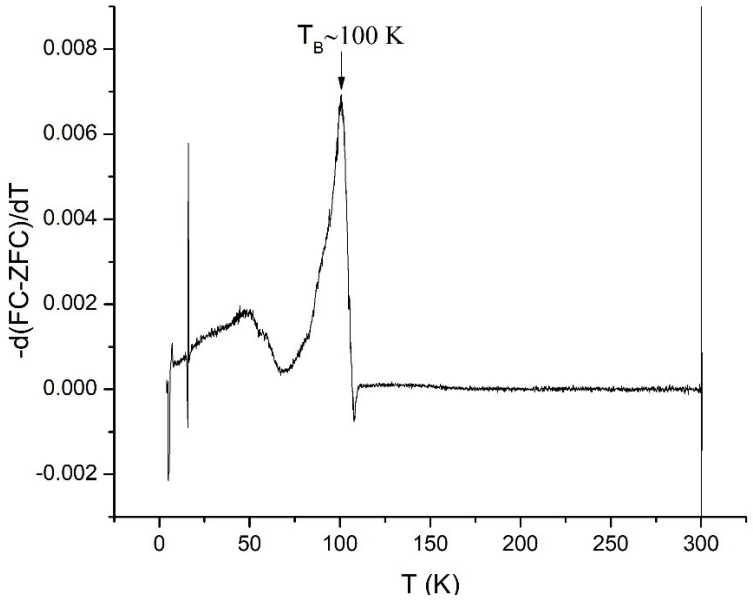

Figure 2.10: Blocking temperature of sample B3

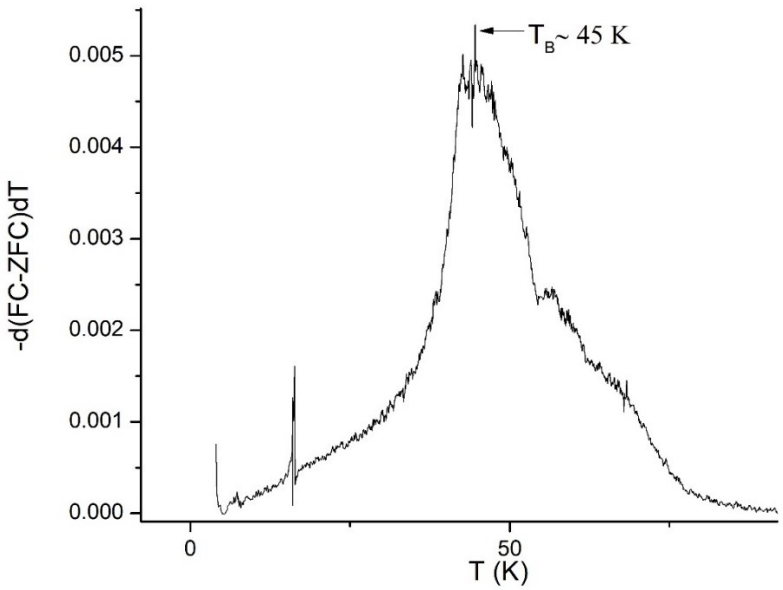

Figure 2.11: Blocking temperature of sample B5

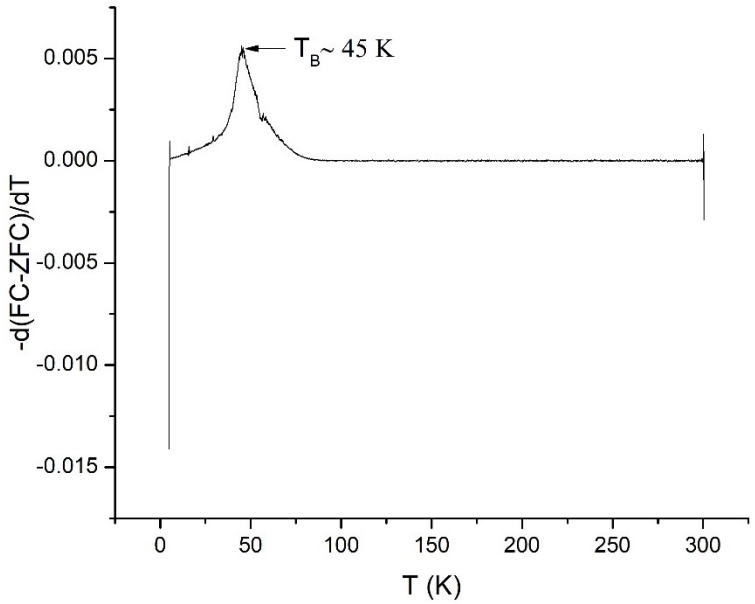

Figure 2.12: Blocking temperature of sample B7

Conclusion

The size of the magnetic heterostructured nanocrystals is dependent on the pH of the synthesis medium as it controls the adsorption of the surrounding material. XRD data reveals that at a pH range of 2.5-8, there are two types of coating over AFM NiO core- (i) $Mn_xNi_{1-x}O$ shell with the same rocksalt structure as NiO and (ii) Mn_3O_4 islands with a spinel structure. Both XRD and TEM data show that the MHNCs surrounding layer over NiO nanoparticles varies with pH and there is a trend in this variation. Our magnetic data confirms that at higher pH there are more Mn_3O_4 than the $Mn_xNi_{1-x}O$ and at a certain point $Mn_xNi_{1-x}O$ shell region ceases to exist. On the other hand, at lower pH, the amount of Mn_3O_4 is noticeably lower than the $Mn_xNi_{1-x}O$ content and they coexist at the middle range of pH values. Again, at higher pH values particles tend to form single domains inducing enhanced coercivity, exchange bias, and magnetization values. The highest magnetization data was found at a pH of 5.03.

References

[1] R. Scarfiello, C. Nobile, and P. D. Cozzoli, "Colloidal magnetic heterostructured nanocrystals with asymmetric topologies: Seeded-growth synthetic routes and formation mechanisms," *Front. Mater.*, vol. 3, no. December, pp. 1–29, 2016, doi: 10.3389/fmats.2016.00056.

[2] N. J. Borys, M. J. Walter, J. Huang, D. V. Talapin, and J. M. Lupton, "The Role of Particle Morphology in Interfacial Energy Transfer in CdSe/CdS Heterostructure Nanocrystals," *Science (80-.).*, vol. 330, no. 6009, pp. 1371–1374, Dec. 2010, doi: 10.1126/science.1198070.

[3] A. Lopez-Ortega *et al.*, "Size-dependent passivation shell and magnetic properties in antiferromagnetic/ferrimagnetic core/shell MnO nanoparticles," *J. Am. Chem. Soc.*, vol. 132, no. 27, pp. 9398–9407, 2010, doi: 10.1021/ja1021798.

[4] Y. X. Wang *et al.*, "Outstanding Comprehensive Performance of La(Fe, Si)13Hy/In

Composite with Durable Service Life for Magnetic Refrigeration," *Adv. Electron. Mater.*, vol. 4, no. 5, pp. 1–8, 2018, doi: 10.1002/aelm.201700636.

[5] K. Chatterjee, S. Sarkar, K. Jagajjanani Rao, and S. Paria, "Core/shell nanoparticles in biomedical applications," *Adv. Colloid Interface Sci.*, vol. 209, pp. 8–39, Jul. 2014, doi: 10.1016/j.cis.2013.12.008.

[6] A. Chakraborty, "Effects of nanoscale inhomogeneities on the magnetic properties of diluted magnetic systems," no. October, 2016.

[7] M. Ghosh, K. Biswas, A. Sundaresan, and C. N. R. Rao, "MnO and NiO nanoparticles: Synthesis and magnetic properties," *J. Mater. Chem.*, vol. 16, no. 1, pp. 106–111, 2006, doi: 10.1039/b511920k.

[8] M. D. Hossain, R. A. Mayanovic, R. Sakidja, M. Benamara, and R. Wirth, "Magnetic properties of core-shell nanoparticles possessing a novel Fe(II)-chromia phase: An experimental and theoretical approach," *Nanoscale*, vol. 10, no. 4, pp. 2138–2147, 2018, doi: 10.1039/c7nr04770c.

[9] N. Thielemann-Kühn *et al.*, "Ultrafast and Energy-Efficient Quenching of Spin Order: Antiferromagnetism Beats Ferromagnetism," *Phys. Rev. Lett.*, vol. 119, no. 19, pp. 1–6, 2017, doi: 10.1103/PhysRevLett.119.197202.

[10] A. B. Shick, S. Khmelevskyi, O. N. Mryasov, J. Wunderlich, and T. Jungwirth, "Spin-orbit coupling induced anisotropy effects in bimetallic antiferromagnets: A route towards antiferromagnetic spintronics," *Phys. Rev. B - Condens. Matter Mater. Phys.*, vol. 81, no. 21, pp. 1–4, 2010, doi: 10.1103/PhysRevB.81.212409.

[11] Y. J. Zhang *et al.*, "Interfacial orbital preferential occupation induced controllable uniaxial magnetic anisotropy observed in Ni/NiO(110) heterostructures," *npj Quantum Mater.*, vol. 2, no. 1, pp. 1–7, 2017, doi: 10.1038/s41535-017-0020-0.

[12] A. C. Johnston-Peck, J. Wang, and J. B. Tracy, "Synthesis and Structural and Magnetic Characterization of Ni(Core)/NiO(Shell) Nanoparticles," *ACS Nano*, vol. 3, no. 5, pp. 1077–1084, May 2009, doi: 10.1021/nn900019x.

[13] Y. T. Chow, B. H. Jiang, C. H. T. Chang, and J. S. Tsay, "Enhancing the magnetic anisotropy energy by tuning the contact areas of Ag and Ni at the Ag/Ni interface," *Phys. Chem. Chem. Phys.*, vol. 20, no. 3, pp. 1504–1512, 2018, doi: 10.1039/c7cp07153a.

[14] F. Luis *et al.*, “Tuning the magnetic anisotropy of Co nanoparticles by metal capping,” *Europhys. Lett.*, vol. 76, no. 1, pp. 142–148, 2006, doi: 10.1209/epl/i2006-10242-2.

[15] S. Rohart *et al.*, “Interface effect on the magnetic anisotropy of CoPt clusters,” *J. Magn. Magn. Mater.*, vol. 316, no. 2 SPEC. ISS., pp. 355–359, 2007, doi: 10.1016/j.jmmm.2007.02.147.

[16] S. Hasan, R. A. Mayanovic, and M. Benamara, “Synthesis and Characterization of Novel Inverted NiO @ Ni x Mn 1-x O Core-Shell Nanoparticles,” *MRS Adv.*, vol. 2, no. 56, pp. 3465–3470, Jun. 2017, doi: 10.1557/adv.2017.445.

[17] E. Demangeat *et al.*, “Colloidal and chemical stabilities of iron oxide nanoparticles in aqueous solutions: The interplay of structural, chemical and environmental drivers,” *Environ. Sci. Nano*, vol. 5, no. 4, pp. 992–1001, 2018, doi: 10.1039/c7en01159h.

[18] G. M. Ullmann, “Relations between protonation constants and titration curves in polyprotic acids: A critical view,” *J. Phys. Chem. B*, vol. 107, no. 5, pp. 1263–1271, 2003, doi: 10.1021/jp026454v.

[19] T. Zhou, J. W. Zha, R. Y. Cui, B. H. Fan, J. K. Yuan, and Z. M. Dang, “Improving dielectric properties of BaTiO3/ferroelectric polymer composites by employing surface hydroxylated BaTiO3 nanoparticles,” *ACS Appl. Mater. Interfaces*, vol. 3, no. 7, pp. 2184–2188, 2011, doi: 10.1021/am200492q.

[20] W. Stumm, “The Inner-Sphere Surface Complex,” 1995, pp. 1–32.

[21] N. Kohli, A. Hastir, and R. C. Singh, “Gas sensing behaviour of Cr2O3 and W6+: Cr2O3 nanoparticles towards acetone,” *AIP Conf. Proc.*, vol. 1731, pp. 10–13, 2016, doi: 10.1063/1.4947698.

[22] N. Ghobadi and F. Khazaie, “Fundamental role of the pH on the nanoparticle size and optical band gap in cobalt selenide nanostructure films,” *Opt. Quantum Electron.*, vol. 48, no. 2, pp. 1–8, 2016, doi: 10.1007/s11082-016-0447-8.

[23] R. Singh and S. Dutta, “Synthesis and characterization of solar photoactive TiO2 nanoparticles with enhanced structural and optical properties,” *Adv. Powder Technol.*, vol. 29, no. 2, pp. 211–219, 2018, doi: 10.1016/j.apt.2017.11.005.

[24] R. Ikono, P. R. Akwalia, W. B. W, A. Sukarto, and N. T. Rochman, “Ikono, R., Akwalia,

P. R., W, W. B., Sukarto, A., & Rochman, N. T. (2012). Effect of PH Variation on Particle Size and Purity of Nano Zinc Oxide Synthesized by Sol-Gel Method, (6), 10–14.Effect of PH Variation on Particle Size and Purity of Nano Zinc Oxid," no. 06, pp. 10–14, 2012.

[25] M. El-Kemary, N. Nagy, and I. El-Mehasseb, "Nickel oxide nanoparticles: Synthesis and spectral studies of interactions with glucose," *Mater. Sci. Semicond. Process.*, vol. 16, no. 6, pp. 1747–1752, 2013, doi: 10.1016/j.mssp.2013.05.018.

[26] S. Dey, M. D. Hossain, R. A. Mayanovic, R. Wirth, and R. A. Gordon, "Novel highly ordered core–shell nanoparticles," *J. Mater. Sci.*, vol. 52, no. 4, pp. 2066–2076, 2017, doi: 10.1007/s10853-016-0495-2.

[27] M. D. Hossain, R. A. Mayanovic, R. Sakidja, and M. Benamara, "An experimental and theoretical study of the optical, electronic, and magnetic properties of novel inverted α-Cr2O3atα-Mn0.35Cr1.65O2.94 core shell nanoparticles," *J. Mater. Res.*, vol. 32, no. 2, pp. 269–278, 2017, doi: 10.1557/jmr.2016.504.

[28] K. Persson, "Materials Data on NiO (SG:225) by Materials Project," 2014. [Online]. Available: https://materialsproject.org/materials/mp-19009/.

[29] K. Persson, "Materials Data on Mn3O4 (SG:141) by Materials Project," 2014. [Online]. Available: https://materialsproject.org/materials/mp-18759/.

[30] P. Gibot and L. Laffont, "Hydrophilic and hydrophobic nano-sized Mn3O4 particles," *J. Solid State Chem.*, vol. 180, no. 2, pp. 695–701, 2007, doi: 10.1016/j.jssc.2006.11.024.

[31] R. Kayestha, Sumati, and K. Hajela, "ESR studies on the effect of ionic radii on displacement of Mn2+ bound to a soluble β-galactoside binding hepatic lectin," *FEBS Lett.*, vol. 368, no. 2, pp. 285–288, 1995, doi: 10.1016/0014-5793(95)00673-W.

[32] R. D. Shannon, "Revised effective ionic radii and systematic studies of interatomic distances in halides and chalcogenides," *Acta Crystallogr. Sect. A*, vol. 32, no. 5, pp. 751–767, Sep. 1976, doi: 10.1107/S0567739476001551.

[33] P. Mallick, C. Rath, A. Rath, A. Banerjee, and N. C. Mishra, "Antiferro to superparamagnetic transition on Mn doping in NiO," *Solid State Commun.*, vol. 150, no. 29–30, pp. 1342–1345, 2010, doi: 10.1016/j.ssc.2010.05.003.

[34] C. A. BARRETT and E. B. EVANS, “Solid Solubility and Lattice Parameter of NiO-MnO,” *J. Am. Ceram. Soc.*, vol. 47, no. 10, pp. 533–533, 1964, doi: 10.1111/j.1151-2916.1964.tb13806.x.

[35] W. Wei, W. Chen, and D. G. Ivey, “Rock salt-spinel structural transformation in anodically electrodeposited Mn-Co-O nanocrystals,” *Chem. Mater.*, vol. 20, no. 5, pp. 1941–1947, 2008, doi: 10.1021/cm703464p.

[36] A. E. Berkowitz *et al.*, “Antiferromagnetic MnO nanoparticles with ferrimagnetic Mn3 O4 shells: Doubly inverted core-shell system,” *Phys. Rev. B - Condens. Matter Mater. Phys.*, vol. 77, no. 2, pp. 1–6, 2008, doi: 10.1103/PhysRevB.77.024403.

[37] T. Ramaprasad, R. J. Kumar, U. Naresh, M. Prakash, D. Kothandan, and K. C. B. Naidu, “Effect of pH value on structural and magnetic properties of CuFe2O4 nanoparticles synthesized by low temperature hydrothermal technique,” *Mater. Res. Express*, vol. 5, no. 9, 2018, doi: 10.1088/2053-1591/aad860.

[38] M. Klinger, *CrysTBox - Crystallographic Toolbox*. Prague: Institute of Physics of the Czech Academy of Sciences, 2015.

[39] J. A. De Toro *et al.*, “A nanoparticle replica of the spin-glass state,” *Appl. Phys. Lett.*, vol. 102, no. 18, 2013, doi: 10.1063/1.4804187.

[40] S. D. Tiwari and K. P. Rajeev, “Signatures of spin-glass freezing in NiO nanoparticles,” *Phys. Rev. B - Condens. Matter Mater. Phys.*, vol. 72, no. 10, pp. 1–9, 2005, doi: 10.1103/PhysRevB.72.104433.

[41] Y. Ichiyanagi, T. Yamada, Y. Kanazawa, and T. Uehashi, “Magnetic properties of Mn3O4 nanoparticles,” *AIP Conf. Proc.*, vol. 850, pp. 1155–1156, 2006, doi: 10.1063/1.2355113.

[42] C. Shell, M. Mn, G. Salazar-alvarez, J. Sort, S. Surin, and M. D. Baro, “Synthesis and Size-Dependent Exchange Bias in Inverted material is cooled below the Curie temperature , T C , and above,” no. 4, pp. 9102–9108, 2007.

[43] J. C. Denardin *et al.*, “Thermoremanence and zero-field-cooled/field-cooled magnetization study of (formula presented) granular films,” *Phys. Rev. B - Condens. Matter Mater. Phys.*, vol. 65, no. 6, pp. 1–8, 2002, doi: 10.1103/PhysRevB.65.064422.

[44] M. Tadic, D. Nikolic, M. Panjan, and G. R. Blake, “Magnetic properties of NiO (nickel

oxide) nanoparticles: Blocking temperature and Néel temperature," *J. Alloys Compd.*, vol. 647, pp. 1061–1068, 2015, doi: 10.1016/j.jallcom.2015.06.027.

[45] O. Kahn, "The magnetic turnabout," *Nature*, vol. 399, no. 6731, pp. 21–23, 1999, doi: 10.1038/19862.

[46] M. I. Shloimys, "Hitchhiker ' s Guide to Magnetism," *Environ. Magn. Work.*, vol. 279, no. 1, p. 48, 1974, doi: 10.1038/nm1005-1051.

[47] A. H. Morrish, *The Physical Principles of Magnetism*. IEEE, 2001.

[48] M. Desai *et al.*, "Anomalous variation of coercivity with annealing in nanocrystalline NiZn ferrite films," *J. Appl. Phys.*, vol. 91, no. 10 I, pp. 7592–7594, 2002, doi: 10.1063/1.1447504.

[49] N. Fontaíña Troitiño, B. Rivas-Murias, B. Rodríguez-González, and V. Salgueiriño, "Exchange Bias Effect in CoO@Fe 3 O 4 Core–Shell Octahedron-Shaped Nanoparticles," *Chem. Mater.*, vol. 26, no. 19, pp. 5566–5575, Oct. 2014, doi: 10.1021/cm501951u.

[50] J. Y. Ji, P. H. Shih, T. S. Chan, Y. R. Ma, and S. Y. Wu, "Magnetic Properties of Cluster Glassy Ni/NiO Core–Shell Nanoparticles: an Investigation of Their Static and Dynamic Magnetization," *Nanoscale Res. Lett.*, vol. 10, no. 1, 2015, doi: 10.1186/s11671-015-0925-0.

[51] M. Rickart, T. Mewes, S. O. Demokritov, B. Hillebrands, and M. Scheib, "Correlation between topography and magnetic surface anisotropy in epitaxial Fe films on vicinal-to-(001) Au surfaces with different step orientation," *Phys. Rev. B - Condens. Matter Mater. Phys.*, vol. 70, no. 6, pp. 1–4, 2004, doi: 10.1103/PhysRevB.70.060408.

[52] G. Salazar-Alvarez *et al.*, "Cubic versus spherical magnetic nanoparticles: The role of surface anisotropy," *J. Am. Chem. Soc.*, vol. 130, no. 40, pp. 13234–13239, 2008, doi: 10.1021/ja0768744.

[53] H. Kachkachi and E. Bonet, "Surface-induced cubic anisotropy in nanomagnets," *Phys. Rev. B - Condens. Matter Mater. Phys.*, vol. 73, no. 22, pp. 1–7, 2006, doi: 10.1103/PhysRevB.73.224402.

[54] R. K. Zheng, G. H. Wen, K. K. Fung, and X. X. Zhang, "Giant exchange bias and the vertical shifts of hysteresis loops in γ-Fe2O3-coated Fe nanoparticles," *J. Appl. Phys.*, vol.

95, no. 9, pp. 5244–5246, May 2004, doi: 10.1063/1.1687987.

[55] X. He *et al.*, “Large exchange bias and enhanced coercivity in strongly-coupled Ni/NiO binary nanoparticles,” *RSC Adv.*, vol. 9, no. 52, pp. 30195–30206, 2019, doi: 10.1039/c9ra03242h.

[56] E. Lottini *et al.*, “Strongly Exchange Coupled Core|Shell Nanoparticles with High Magnetic Anisotropy: A Strategy toward Rare-Earth-Free Permanent Magnets,” *Chem. Mater.*, vol. 28, no. 12, pp. 4214–4222, 2016, doi: 10.1021/acs.chemmater.6b00623.

[57] J. Nogués *et al.*, “Exchange bias in nanostructures,” *Phys. Rep.*, vol. 422, no. 3, pp. 65–117, 2005, doi: 10.1016/j.physrep.2005.08.004.

[58] H. Zabel and S. D. Bader, *Magnetic Heterostructures*, vol. 227, no. 5. Berlin, Heidelberg: Springer Berlin Heidelberg, 2008.

[59] E. F. Kneller and F. E. Luborsky, “Particle size dependence of coercivity and remanence of single-domain particles,” *J. Appl. Phys.*, vol. 34, no. 3, pp. 656–658, 1963, doi: 10.1063/1.1729324.

[60] X. Batlle, M. García Del Muro, J. Tejada, H. Pfeiffer, P. Görnert, and E. Sinn, “Magnetic study of M-type doped barium ferrite nanocrystalline powders,” *J. Appl. Phys.*, vol. 74, no. 5, pp. 3333–3340, 1993, doi: 10.1063/1.354558.

[61] B. P. Toperverg and H. Zabel, “Neutron Scattering in Nanomagnetism,” in *Experimental Methods in the Physical Sciences*, vol. 48, Elsevier, 2015, pp. 339–434.

[62] S. W. Chen *et al.*, “Nonswitchable magnetic moments in polycrystalline and (111)-epitaxial permalloy/CoO exchange-biased bilayers,” *Phys. Rev. B - Condens. Matter Mater. Phys.*, vol. 89, no. 9, 2014, doi: 10.1103/PhysRevB.89.094419.

CHAPTER 3: XPS ANALYSIS OF MN_3O_4 AND/OR MN_XNI_{1-X} O SURROUNDED NIO HETEROSTRUCTURED NANOCRYSTALS AS A FUNCTION OF SYNTHESIS MEDIUM pH

Abstract

Hydrothermal and thermal evaporation method was used to synthesize NiO based heterostructured nanocrystals surrounded by Mn_3O_4 islands and/or $Mn_xNi_{1-x}O$ shell at different pH levels (2.5-7) of the synthesis medium. The surface composition of the nanocrystals was examined by x-ray photoelectron spectrometry (XPS) for all the NiO nanoparticles and the heterostructured nanocrystals. The auger electron effect data found in the NiO nanoparticle samples were employed to interpret the manganese 2p region as both the manganese 2p region and Ni auger peak region fall in the same XPS spectra. XPS analysis of all the nanocrystal samples yields a trend having a higher amount of Mn_3O_4 islands at higher pH, a higher amount of $Mn_xNi_{1-x}O$ shell in the lower pH and a mixture of both in between. Our high-resolution TEM image and XRD data analysis shows consistency with the XPS results. The nanocrystals predominantly show faceted structure where the Mn_3O_4 islands form perpendicularly over the facets whereas the shell region forms in a discontinuous manner surrounding the nanoparticle. It has been also found that the pH of the synthesis medium affects the adsorption of Mn^{2+} and Mn^{3+} ions as well as the morphology of the structure.

Introduction

The field of nanocrystals owing to the advance of chemistry and materials science has been attracting greater attention because of the versatility of their physical and chemical

properties. Along with the shape, the discovery of the size and structure dependence of the nanocrystals has guided the way for a complex and sophisticated multi-layered, multi-component structure known as heterostructured nanocrystals (HNCs) [1]–[3]. The HNCs, bonded by direct solid-state chemical heterointerfaces are fabricated to overcome the challenges posed by conventional nanoparticles. Controlled synthesis of the nanocrystals has led to the architectural control of the shape and adjustable properties which can be manipulated to use in numerous applications. For example, the magnetic heterostructured nanocrystals (MHNCs) exhibit unique nanoscale magnetic behaviors such as enhanced coercivity, increased saturation magnetization and magnetic exchange bias which can be tailored for novel magneto-optical or spintronic devices [4]–[6]. The MHNCs have been widely adopted for electronic applications such as FET, memory device, solar cell, photovoltaics and lasers [4], [7]. The MHNCs also provide notable scopes for biomedical applications because of their optimization of size and controllable manipulation by an external magnetic field. One of the noteworthy application of MHNCs in nanobiotechnology is the drug delivery followed by the use as an MRI agent, biosensors, multimodal imaging, and magnetophoresis experiments [8]–[11]. One of the most fascinating branches of MHNCs is the transition metal oxides based magnetic heterostructured nanocrystals which show phenomenal magnetic, electric and catalytic properties [12]–[14]. Besides, the transition metal oxide-based MHNCs exhibit fast resistance switching phenomena which are very much effective for making nonvolatile memory devices [15], [16]. Also, these kinds of MHNCs show high Curie temperature, T_c overcoming superparamagnetic limit and a wide range of ferromagnetic to paramagnetic behavior [17], [18]. Although NiO is an antiferromagnetic rocksalt structured transition material, incorporation of manganese oxides into/over NiO either as a coating, doping or distinct layer introduces an enormous change in physical and chemical

properties [19]–[22]. It has been seen in our previous study that the magnetic nature of the complex heterostructured system of NiO with Mn_3O_4 islands and/or $Mn_xNi_{1-x}O$ shell contains ferrimagnetism and results in higher coercivity and exchange bias [23], [24]. But it is still unclear how much Mn_3O_4 and/or $Mn_xNi_{1-x}O$ shell are present in the system at different pH levels which are considered to be the source of the ferrimagnetic behavior. Also, the magnetic data analysis via PPMS or SQUID does not give tangible data to envisage the effect of pH on the structural change of the MHNCs.

During the hydrothermal synthesis process, Mn^{2+} and Mn^{3+} ions are adsorbed over the NiO surface competing with the highly reactive OH^- ions present in the aqueous solutions. The adsorption and growth of the ions over the metallic oxide surface can be controlled via the protonation and deprotonation process explained thoroughly in previous literature [25]–[29]. As protonation or deprotonation reactions are highly modified by the pH of the aqueous solutions, the adsorption rate of the metallic ions becomes dependent on the solution pH. As a result, pH can affect the structural composition as well as the shape of the resultant nanocrystals owing to the growth of metallic ions in a particular direction [30]–[32]. Eight different samples synthesized at a pH range of 2.34 to 7 have been synthesized to understand this effect. The nature of the morphological and structural change of Mn_3O_4 and/or $Mn_xNi_{1-x}O$ surrounded NiO magnetic heterostructured nanocrystals with respect to pH change during the synthesis process will be explored in the following discussions. To get fresh insights about these complex issues X-ray photoelectron spectrometry (XPS) along with XRD and TEM analysis has been done on three NiO nanoparticle samples and eight MHNCs samples.

According to the National Institute of Standards and Technology (NIST) XPS database, the binding energy for 2p 3/2 region for oxides of manganese whether it is MnO, Mn_2O_3 or

Mn_3O_4 falls between 640.40 eV to 642.80 eV [33]. On the other hand, the Auger electron peaks for the Ni 2p region fall between 636.3 eV to 643.10 eV of binding energy. As a result, Ni auger peaks merge and suppress the Mn 2p 3/2 peaks and it becomes difficult to identify the later peaks. There are not a lot of available discussion on how to identify the Mn 2p 3/2 peaks and associated area in this kind of situation. Our approach to overcome this difficulty is to use the Ni Auger peaks for NiO nanoparticle samples (which does not have any manganese) and use the same data - location of the peaks, full-width half max (FWHM) value and the area ratio between multiple peaks into MHNCs XPS fitting. We have also maintained the peak area ratio of 1:2 between Mn 2p 1/2 and Mn 2p 3/2 peaks to further bolster the fitting for the later one. The quantitative analysis of the structural components was calculated following this approach of peak fitting. It has been also considered that some Ni-OH bonds occur in the aqueous solution and show up in the O 1s region peak.

Experimental

The NiO nanoparticles (labeled as A1, A2, A4 or A5) were synthesized first via thermal decomposition technique suggested by El Kemary et. al. where $Ni(OH)_2$ decomposed into NiO powders at 600ºC [34]. The $Ni(OH)_2$ powder was formed by the reaction of $NiCl_2.6H_2O$, NaOH and $N_2H_4.H_2O$ taken at a ratio of 1:5:10. They were added with absolute ethanol solution and mixed for about 3hrs using a magnetic stirrer. The molar concentration of the $NiCl_2.6H_2O$ was maintained at 0.11M. After proper mixing of all the constituents, $Ni(OH)_2$ was formed as a precipitate at the bottom of the beaker via the following reactions.

$$NiCl_2.6H_2O + 6C_2H_5OH \rightarrow [Ni(C_2H_5OH)_6]Cl_2$$

$[Ni(C_2H_5OH)_6]Cl_2 + mN_2H_4 \rightarrow 6C_2H_5OH + [Ni(N_2H_4)m]Cl_2$

$[Ni(N_2H_4)m]Cl_2 + 2KOH \rightarrow mN_2H_4 + Ni(OH)_2$

After careful extraction, the $Ni(OH)_2$ powders were placed in an oven at 600°C for 2 hours where it transformed into NiO powder [$Ni(OH)_2 \rightarrow NiO + H_2O$]. This NiO powder at an amount of 0.33gm was added with 0.5M $MnCl_2.3H_2O$ to produce the MHNCs by hydrothermal process delineated by others [24][35], [36]. But before this addition, the $MnCl_2.3H_2O$ was taken into deionized water that was purged with N_2 gas at 65-70°C for 15-20 minutes. Also, the pH of the solution of the deionized water and $MnCl_2.3H_2O$ mixture was measured and altered by using HCl or NaOH. After NiO powder addition, the whole mixture was sonicated for 25-30 minutes and put in an autoclave which was then placed in an oven at 200°C temperature for 22.5hrs. Once the MHNCs were formed in the autoclave, it was then washed thoroughly with DI water and dried to get the final samples. Table 3.1 lists all the samples that were synthesized at different pH values.

Table 3.1: List of samples synthesized at various solution pH and the particle size from XRD

Sample	B1	B2	B3	B4	B5	B6	B7	B8
pH	2.39	2.98	3.52	4.02	4.48	5.03	6.02	7.03
size (nm) from XRD	29.34	29.69	28.74	29.24	25.03	27.74	25.53	24.89

The structure of the MHNCs was characterized by x-ray diffraction (XRD) using Bruker D8 Discover diffractometer machine and Cu Kα radiation (λ = 1.54184Å). The XRD machine operates at 40kV and 40mA, has a Gobel mirror and 0.6mm slit mounted in front of the detector. The nanoparticle samples were taken over a glass slide and the ethanol that had been used as a

solvent was allowed to evaporate before putting the samples into the machine. The samples were scanned from 20 to 70^{o} at 2θ range and 0.01^{o} increment with 4 second/step scan speed. The XRD patterns were further analyzed by Rietveld refinement using TOPAS software by Bruker. The XPS analysis was done using Versa Probe XPS from Physical Electronics with monochromated K alpha x-rays from aluminum at 1486 eV. 117.4 eV pass energy was used for survey scans and 58.7 eV or below pass energy was used for high-resolution scans. The source and analyzer of the XPS instrument were calibrated using the Ag $3d_{5/2}$ (FWHM=0.36 eV) peak having characteristic energy of 368.26 eV. An Alpha 110 hemispherical analyzer (Thermo Scientific) having pass energy of 25 eV was used to collect the x-ray photoelectron spectra. High-resolution XPS scan were done in 840-890 eV (binding energy) for Ni 2p region, 520-540eV (binding energy) for O 1s region and 626-660 eV (binding energy) for Ni Auger/ Mn 2p region. XPS data analysis and peak fitting were performed using CasaXPS 2.3.16 software and the calibration using a carbon 1s peak (284.8 eV) from carbon tape. For quantitative analysis, the software uses corrected Relative Sensitivity Factor (RSF) values of 93.683 for Ni2p, 16.732 for O1s, 67.281 for the Mn2p region. TEM samples were prepared using hexane as a solvent and a probe sonicator for proper dispersion of the nanocrystals. The samples were taken over the carbon lacey grids and the hexane was allowed to dry out of the samples. Images and data were collected using a G2 F20 X-Twin (TECNAI) microscope located at the GeoForschungZentrum, Potsdam, Germany. The images were post analyzed by ImageJ software for the region selection, size determination and FTIR analysis.

Results and discussion

Bulk Mn_3O_4 (hausmannite) is a spinel structured material where the octahedral sites are occupied by Mn^{3+} and the tetrahedral sites are occupied by the remaining Mn^{2+} [37], [38]. On the other hand, $Mn_xNi_{1-x}O$ shell carries the same rocksalt structure as NiO as it originates from MnO which has the same crystal structure as NiO [22], [23]. The lattice parameters (a) of NiO and MnO are 4.17 Å and 4.44 Å respectively while Mn_3O_4 has a lattice parameter of a = 5.72 Å and c = 9.35 Å [37]–[40]. The ionic radius of Ni^{2+} and Mn^{2+} are different from each other in an extent of 0.03 Å (Ni^{2+} = 0.69 Å and Mn^{2+} = 0.66 Å) [21]. Figure 3.1 (a) depicts the XRD patterns of sample A2 (NiO nanoparticle), B1, B4, and B8. There are no Mn_3O_4 peaks in A2 and B1 which are visible in B4 and B8 (red color). In Figure 3.1(b), Rietveld refinement of sample A2 (which gives almost the same spectra as B1) and B3 confirm different elements at different pH values as well as show the difference from calculated to experimental values. Table 3.1 shows the particle size of one of the NiO nanoparticle (A2) and of all HNCs that are obtained using Scherrer formula $D = k\lambda/\beta\cos\theta$ [41]. Here D is the particle dimension, K is a constant which is often taken as unity, λ is the x-ray wavelength, β is the peak width and θ is the angle between the beam and the normal on the reflection plane. The clear trend of decreasing particle size with increasing pH values is seen in table 1. Figure 3.1(c) illustrates one of the high-resolution TEM images (B1) where the particles are seen to be in faceted shape. Figure 3.1(d) represents the histogram of sample B1 delineating the particle size of 30.85 nm which is 29.34 from XRD data.

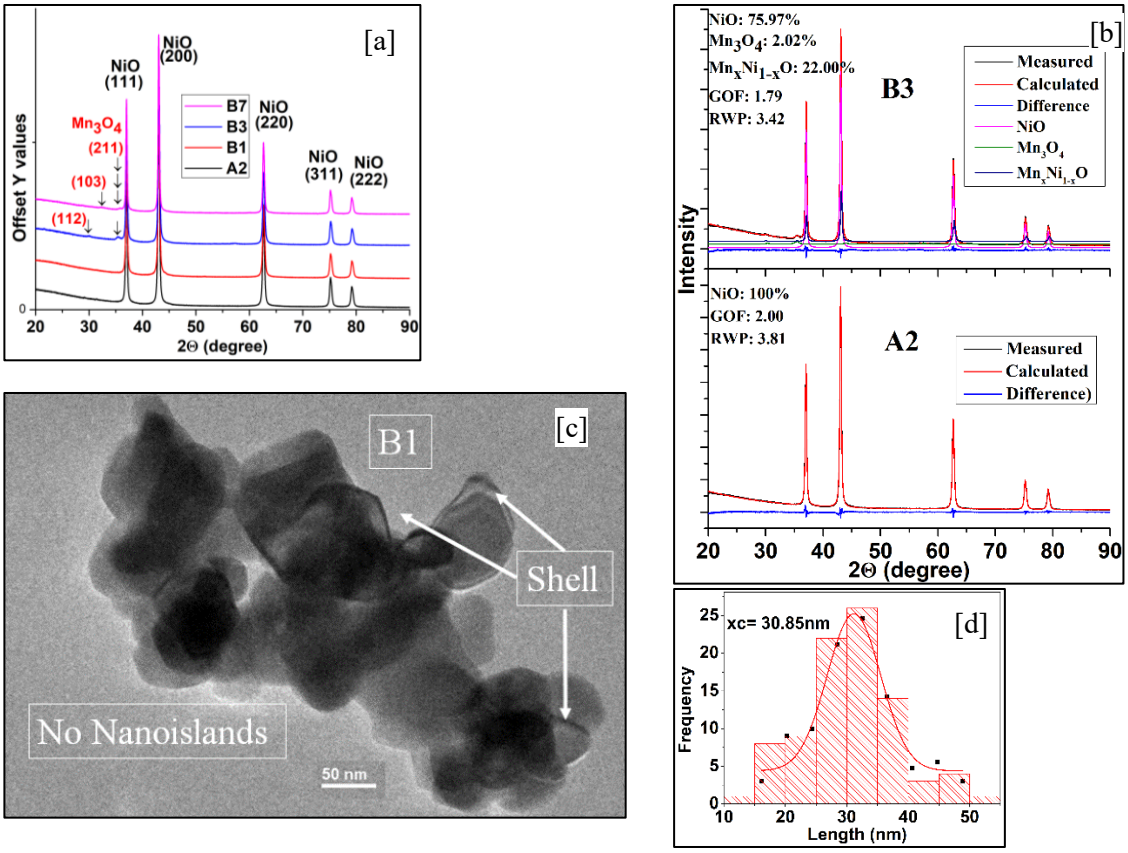

Figure 3.1: (a) XRD peaks of NiO nanoparticle (A2) and of different heterostructured nanocrystals: B1 (pH = 2.39), B3 (pH = 3.52), B7 (pH = 6.02); (b) Rietveld refinement of sample A2 and B3 (c) high resolution TEM image of sample B1, (d) histogram of the particles yields particle size of 30.85 nm.

Due to the structural and ionic size differences, there are some lattice strain and structural reorientation at the interface of different layers of the nanocrystals. Figure 3.2(a) identifies one such crystal reorientation of NiO and Mn_3O_4 (111) plane which results in vacancy defects when Mn_3O_4 grows over NiO nanoparticle. This criterion is also visible in high-resolution TEM images. Figure 3.2 (bottom) shows a similar case of crystal reorientation plus the vacancy defects that are found in the sample B6 MHNC sample at pH = 5.03. A similar case can also occur when Mn_3O_4 builds up on top of the $Mn_xNi_{1-x}O$ shell layer. Figure 3.2(b-e) also provides insights into

the structure by analyzing Fourier-transform infrared spectroscopy (FTIR) at different levels of the sample. The FTIR analysis confirms the presence of different crystal structures vis-à-vis different elements present in the system. The TEM-EDS also falls in line with FTIR results (Figure 3.2).

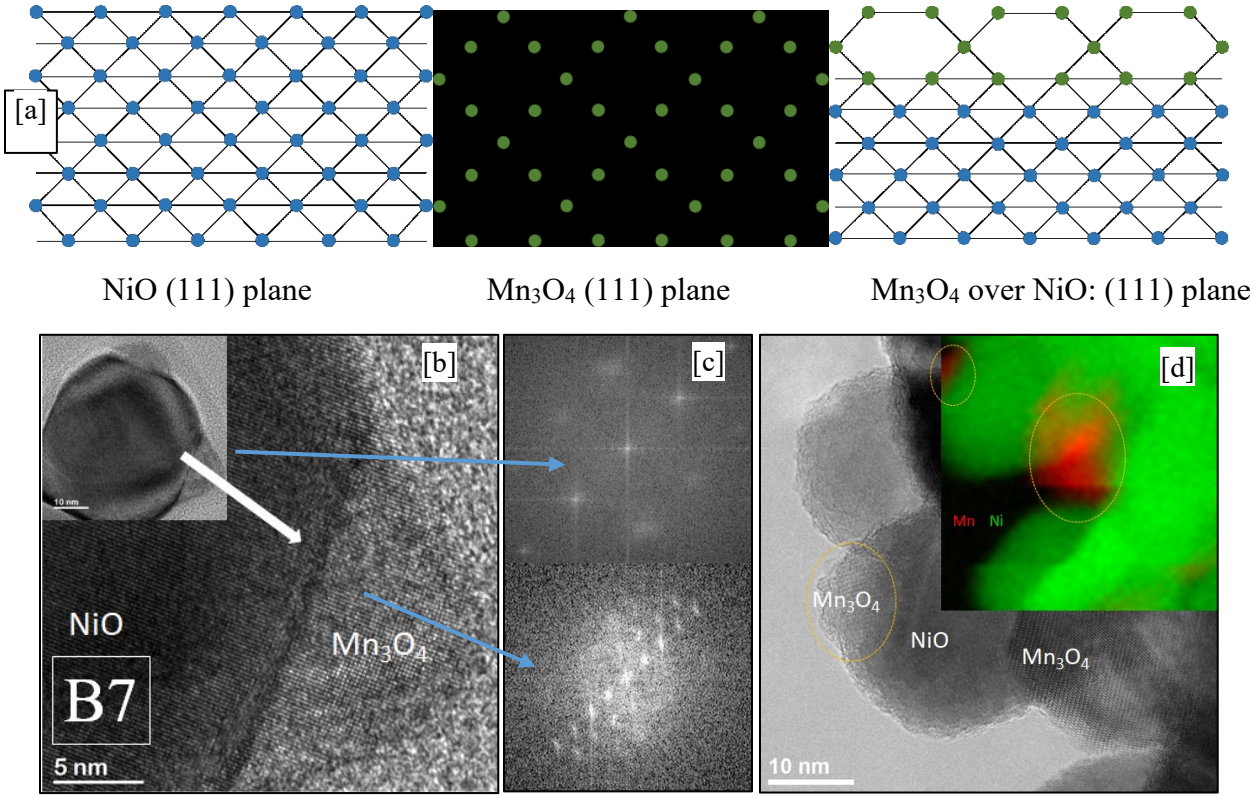

Figure 3.2: (a) 2-dimensional view of NiO, Mn_3O_4 and NiO-Mn_3O_4, (111) plane (b) HRTEM image of sample B7 (pH = 6.02) showing the lattice defect at the interface of two different crystal structure, (c) FTIR image shows the presence of different crystal structure at different position (d) TEM EDS data confirms the presence of two different elements of Mn and Ni.

The Ni 2p XPS spectrum of NiO nanoparticle (A1) and some of the nanocrystals (B1, B3, B5, and B7) are illustrated in Figure 3.3. The 2p region is split into two parts called $2p_{1/2}$ and $2p_{3/2}$ due to spin-orbit coupling. The main peaks of the $2p_{1/2}$ and $2p_{3/2}$ are visible in Figure 3.3 (A1) by the DOT point while the satellite peaks are depicted by the ARROW sign. Satellite

peaks are the resultants of the shake-up effect that happens due to the excitation of the photoelectron and deposition of the energy in the system left by the kinetic energy of that particular photoelectron [42]. In NiO, Ni^{2+} [(Ar) $3d^8$], electrons removed by the x-ray from the 2p region interact with the electrons from 3d shell which generates the satellite peaks in the structure. The relative positions of the mainline and satellite peaks of all the samples shown in the Figure are enlisted in Table 3.2. The peak position of the nanocrystal samples is almost the same as the NiO nanoparticles but the satellite peaks are less distinguishable as the pH of the nanocrystals is increasing. The satellite peaks are situated at approximately 7 eV higher binding energy from the main peak lines. But, according to Biju et. al, there should be another satellite peak from the main lines at a distance of 1.5eV which are prominent in NiO nanoparticle sample (A1) but not very much in nanocrystal samples [43]. According to Wilson et. al., there are a couple of reasons behind the sharp decrease of the satellite structures among which the size of the nanoparticles and defects in the crystal structure are two notable ones [44]. They stated that reduction in satellite intensity is directly related to the decreasing particle size. As the particle size decreases, the large surface to volume ratio increases along with defect density together which affects the shake-up process. This assertion is in good comparison with our observed particle size reduction with increasing pH values. But, the peak at 1.5 eV from $2p_{3/2}$ has been attributed due to multiplet splitting by other authors [45]–[49]. Multiplet splitting occurs if there are unfilled shells with lone pairs like in transition metals with partially filled p and d shells and rare-earth metals with f orbitals. It arises from the fact that an electron can have spin up/down states, which creates 2 states observed as separate peaks in XPS In case of NiO, multiplet splitting is related to both local and non-local screening effects of the final state of the electronic structure resultant of the photoemission process. The lowest energy state for NiO is $2p^5\ 3d^9\ \underline{L}$

which occurs due to the nonlocal screening process of $2p^6\ 3d^8 + h\upsilon \rightarrow 2p^5\ 3d^9\ \underline{L} + e^-$ and this action is considered responsible for the peaks at ~1.5 eV from the main peaks [43], [49]. Here $\underline{L}$ represents a valence band hole whereas the $\underline{2p}$ can be considered as a photon-induced hole in

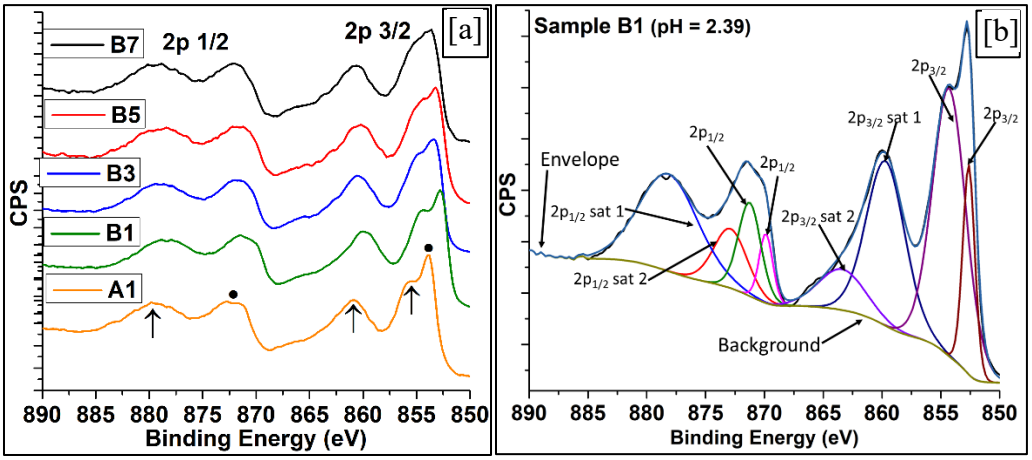

Figure 3.3: (a) XPS spectra of Ni 2p region of some of the nanocrystal samples [B1 (pH = 2.39), B3 (pH = 3.52), B5 (pH = 4.48), B7 (pH = 6.02)] along with the NiO nanoparticle (A1). The arrow sign points to the satellite peaks while dot points the main peaks; (b) detailed peak fitting of the XPS peaks of sample B1.

Table 3.2: peak positions and the binding energy difference between Ni 2p main peaks and satellite peaks

	Peak Positions (Binding Energy, eV)							
	$2p_{3/2}$ 1	$2p_{3/2}$ 2	$2p_{3/2}$ Sat 1	$2p_{3/2}$ Sat 2	$2p_{1/2}$ 1	$2p_{1/2}$ 2	$2p_{1/2}$ Sat 1	$2p_{1/2}$ Sat 2
A1	853.83	855.36	860.91	864.17	872.14	872.72	874.08	879.23
B1	852.63	854.33	859.71	863.12	869.88	871.35	873.20	878.17
B3	853.15	854.79	860.34	864.77	870.46	871.91	873.62	878.71
B5	852.97	854.59	860.15	863.22	870.21	871.44	873.01	878.49
B7	853.38	854.96	860.62	863.72	870.32	871.49	873.11	878.82

another process called local screening ($2p^6\ 3d^8 + h\upsilon \rightarrow \underline{2p}^5\ 3d^8 + e^-$) The mainline peaks at around 853 eV and 871 eV are generated due to this local screening effects. To cover the

multiplet envelops of $2p_{1/2}$ and $2p_{3/2}$ spectra region, 4 different peaks are used for each of them and the fittings are shown in Figure 3.3(b).

The Auger peaks are typically represented by the kinetic energy as the Auger electron does not have binding energy and they are produced by auto-ionization. As a result, the position of the auger electron lines in the XPS spectra does not change with the applied x-ray characteristic energy. Here we have used the binding energy in the figures so that both the Mn $2p_{3/2}$ region and Ni auger spectra can be presented straightforwardly. As stated earlier, the auger peak region of Ni (636.30 eV to 642.10 eV of binding energy) merges with the XPS spectra of the Mn $2p_{3/2}$ region (640.40 eV to 642.80 eV of binding energy) and it is difficult to identify individual peaks of this two elements. We have introduced a simple method to find the Ni auger peaks in pure NiO nanoparticles and using the same data (peak position, peak area ratio and FWHM value) to fit the peaks of Mn $2p_{3/2}$ spectra since we could not find any other established method to solve this issue [46], [50]–[52]. The Ni LMM auger peak is largely dependent on the electronic configuration of Ni and the unoccupied 3d states which arise from $3d^{10}$ initial state and fall into $3d^8$ final state [46][53]. The LMM auger peak is also known as $L_3M_{45}M_{45}$ or L_3VV where M_{45} represents the multiplet combinations of the $3d_{3/2}$ and $3d_{5/2}$ valence electrons and V is valence. The XPS data of Ni auger peaks found from different NiO nanoparticles are employed in table 3.3 which was analyzed using the parameters provided in the NIST database [33]. All the NiO nanoparticle samples (A1, A2, A4, and A5) were synthesized using the same parameters and the average area ratio of the two Ni LMM peaks were calculated as 1.80. The peak position and area ratio of all the NiO nanoparticle samples must stay the same. But from the table, it is clear that they are not the same and there are several reasons for that such as non-local screening effect or the presence of O^{-} or Ni^{3+} as a minor defect. The average peak position, the FWHM

Table 3.3: Auger peak fitting details of NiO nanoparticles and NiO nanocrystals

Sample	Ni LMM Peak 1 Kinetic Energy (eV)	FWHM	Ni LMM Peak 2 Kinetic Energy (eV)	FWHM	Area ratio
NIST data	*849.70*	*4.68*	*842.90*	*7.00*	-
A1	849.91	4.50	844.28	8.36	1.82
A2	849.84	4.24	844.23	8.80	1.83
A4	849.89	4.33	844.25	7.59	1.79
A5	849.60	4.40	843.99	8.55	1.77
B1	850.96	4.12	844.29	7.27	1.75
B2	848.67	4.78	842.94	7.03	1.79
B3	850.13	4.53	844.21	6.90	1.79
B4	849.96	4.50	844.14	6.58	1.80
B5	850.24	4.68	844.50	7.34	1.79
B6	850.75	4.07	844.88	5.92	1.80
B7	850.18	4.46	844.75	6.49	1.78
B8	849.15	4.31	843.87	6.10	1.79

value and the area ratio was further employed to fit the peaks of the nanocrystals. Figure 3.4(b) shows the Ni auger and the Mn $2p_{3/2}$ spectra of some of the nanocrystal samples along with one NiO nanoparticle sample where it is very much clear that the Mn brings up new peaks in nanocrystals. The amount of Mn in sample B1 (pH = 2.39) is comparatively low which can also be confirmed from Figure 3.4(a) of Mn $2p_{1/2}$ spectra. That is why the Mn contribution to Ni auger region is not very subtle like in other samples. The high amount of hydrogen ion in this low pH might have hindered the formation of shell or nanoisland over the NiO nanoparticles. Figure 3.4(c) shows the peak fitting of the NiO nanoparticles and the nanocrystals which authenticate the presence of Mn $2p_{3/2}$ peaks.

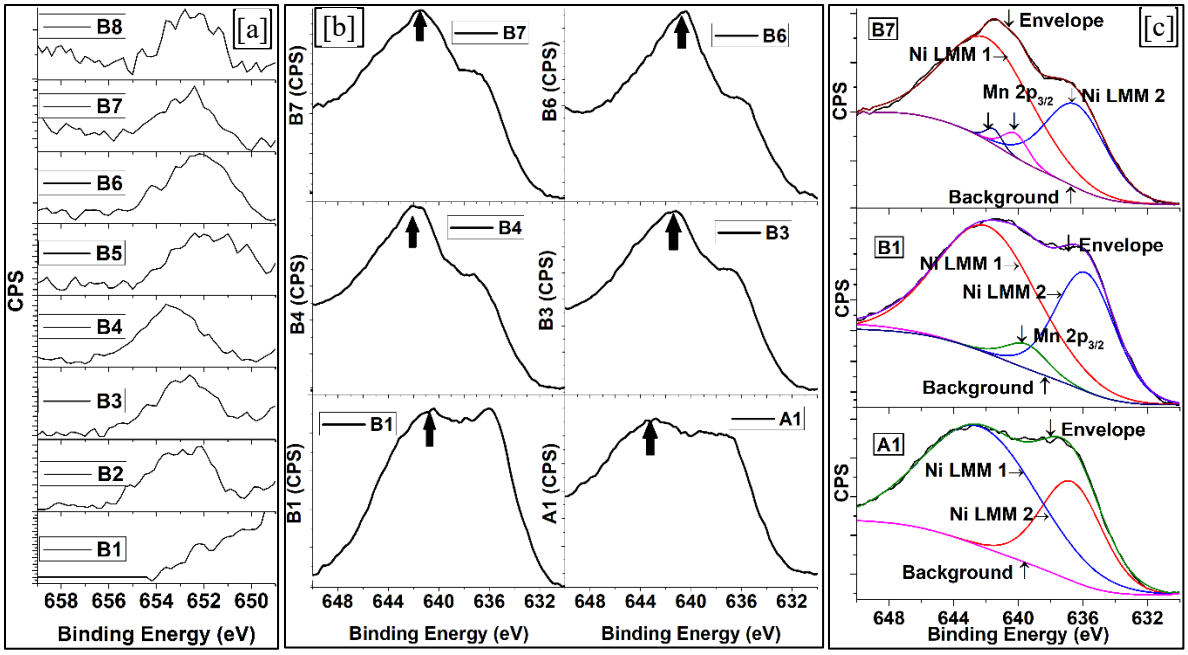

Figure 3.4: (a) XPS spectra of Mn $2p_{1/2}$ region and, (b) Ni auger and Mn $2p_{3/2}$ region of magnetic heterostructured nanocrystals. Arrow sign indicates the peak that is absent in A1, the little contribution of Mn in sample B1 (pH = 2.39) and significant contribution in sample B3, B4, B6, B7. (c) An illustration of the peak fitting for Ni LMM auger peaks and Mn $2p_{3/2}$ peaks.

Most natural oxidation states of Manganese are 2^+, 3^+ and 4^+ while it has several other oxidation states ranging from 7^+ to 3^- [54]. As the pH changes, the oxidation states of the nanocrystals also varies. The reason behind this is the protonation and the adsorption effects that occur simultaneously in the aqueous synthesis solution. As the number of hydrogen ion increases with lower pH, less number of Mn ions get adsorped over the nanoparticle surface while the opposite happens with higher pH. And as the number of Mn ion adsorption is changing from pH variation, the oxidation states of Mn in the nanocrystal samples are also changing. XPS analysis can assess the oxidation states of manganese by measuring the sensitivity of the binding energy of various electron energy levels. Although, according to previous literature, Mn 3s spectra can explore the valence state of manganese oxides more precisely, the energy difference between the Mn $2p_{1/2}$ and $2p_{3/2}$ peaks can also be a good measurement to prove it [55]–[59]. But since the Mn

$2p_{3/2}$ peaks are suppressed due to the Auger spectra of Ni LMM, our focus falls on to the Mn $2p_{1/2}$ region first. From Figure 3.4(a), it is comprehensible that the peak of the $Mn_{1/2}$ region has been aligned for some samples than shifted for some other samples. The standard energy difference between this two peaks are 11.2-11.4 eV for Mn^{2+} and 11.7-11.8 eV for Mn^{3+} oxidation state [55], [57]–[59]. Figure 3.5 illustrates some of the nanocrystal samples' Mn $2p_{1/2}$ and $2p_{3/2}$ peak fittings. It can be seen that the difference of area of Mn $2p_{3/2}$ peaks and Mn $2p_{1/2}$ peaks are higher in sample B7 than any other samples. We can predict that the percentage of Mn^{3+} is higher in higher pH samples. As from table 3.4, the energy difference for B1 is 11.3 eV and for other samples, it varies from 11.3 to 11.6 eV for peak 1 and 11.7 to 12.1 eV for peak 2. From these results and XRD and TEM analysis, we can predict that the sample B1 has only the Mn^{2+} oxides while other samples have both Mn^{2+} and Mn^{3+} states either in the form of Mn_3O_4 only or both Mn_3O_4 and $Mn_xNi_{1-x}O$ shell. Analysis of the Mn 3s spectra can further confirm the oxidation states of manganese.

Table 3.4: Position of the Mn $2p_{1/2}$ and $2p_{3/2}$, 3s multiplet peaks and energy difference

	Peak Position, B.E. (eV)			Peak Position, B.E. (eV)			Peak Position, B.E. (eV)		
	Mn 2p1/2 peak 1	Mn 2p3/2 peak 1	Diff. eV	Mn 2p1/2 peak 2	Mn 2p3/2 peak 2	Diff. eV	Mn 3s peak 1	Mn 3s peak 1	Diff. eV
B1	650.39	639.09	11.3	-	-	-	86.86	78.26	8.6
B2	651.63	640.23	11.4	653.13	641.23	11.9	-	-	-
B3	651.05	639.75	11.3	652.88	641.08	11.8	85.18	79.54	5.6
							87.66	81.14	6.5
B4	652.78	641.28	11.5	654.18	642.48	11.7	86.36	80.79	5.6
							88.57	81.97	6.6
B5	650.90	639.5	11.4	652.75	640.85	11.9	-	-	-
B6	649.97	638.37	11.6	652.23	640.13	12.1	87.22	81.82	5.4
B7	650.98	639.58	11.4	652.62	640.82	11.8	87.29	81.70	5.5
B8	651.47	639.97	11.5	652.82	641.02	11.8	-	-	-

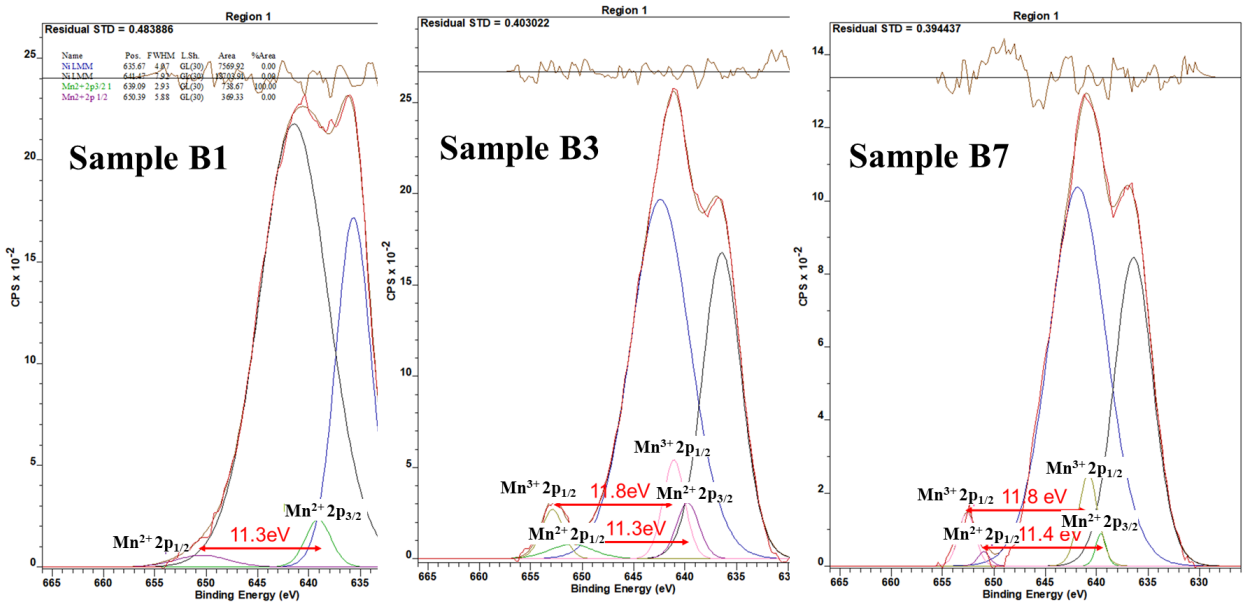

Figure 3.5: Mn 2p XPS spectra of different nanocrystal samples showing Mn $2p_{1/2}$ and $2p_{3/2}$ peaks

In manganese, there is an exchange coupling between the 3s hole and 3d electrons that creates multiplicity proportional to 2S+1 (S is the local spin of the 3d electrons in the ground shell) [56], [60], [61]. The high spin coupled states will be in lower binding energy with multiplicity 2S and low spin coupled states will be in higher binding energy with multiplicity 2S+2. Because of the exchange coupling, there is multiplet splitting in Mn 3s spectra that can vary depending on the oxidation states of manganese. There has been a lot of works on this spectral splitting of Mn 3s in monovalent Mn oxides such as MnO, Mn_2O_3 or Mn_3O_4. The energy differences between the two multiplet peaks of the monovalent oxides have been a clear indicator of the oxidation states of the manganese. It has been reported that the energy difference between two peaks are around 5.8-6.1eV for Mn^{2+}, 5.2-5.5 eV for Mn^{3+} and 4.5-4.7eV for Mn^{4+} [54], [62]–[64]. Figure 3.6 shows the multiplet splitting of some of the nanocrystal samples and table 3.4 shows the peak position and binding energy difference. From table 3.4, we can see that the

energy difference of two multiplet peaks of sample B1 is 8.6 eV and there are two energy differences for sample B3 and B4. Since manganese has several oxidation states, 8.6 eV of energy difference indicates a lower oxidation state than 2^+ [54]. Both B3 and B4 have Mn^{3+} oxides along with possible Mn^{2+} or lower oxides. The physical meaning of these values states that B1, B3, and B4 all have $Mn_xNi_{1-x}O$ but B3 and B4 also have Mn_3O_4 oxides. Similarly, sample B6 and B7 both have only Mn^{3+} oxidation state but there are no lower oxides than Mn_3O_4. According to our TEM and TEM-EDS data, sample B1 has no Mn_3O_4 islands, sample B2 to B4 contains both Mn_3O_4 and $Mn_xNi_{1-x}O$ and sample B5 to B8 contains very little to no $Mn_xNi_{1-x}O$ elements. Since the amount of Mn_3O_4 is comparatively lower than the $Mn_xNi_{1-x}O$ shell, the peaks are not very prominent for the 3^+ oxidation state. Nevertheless, these results are in good comparison with the data found from Mn 3s spectral lines analysis.

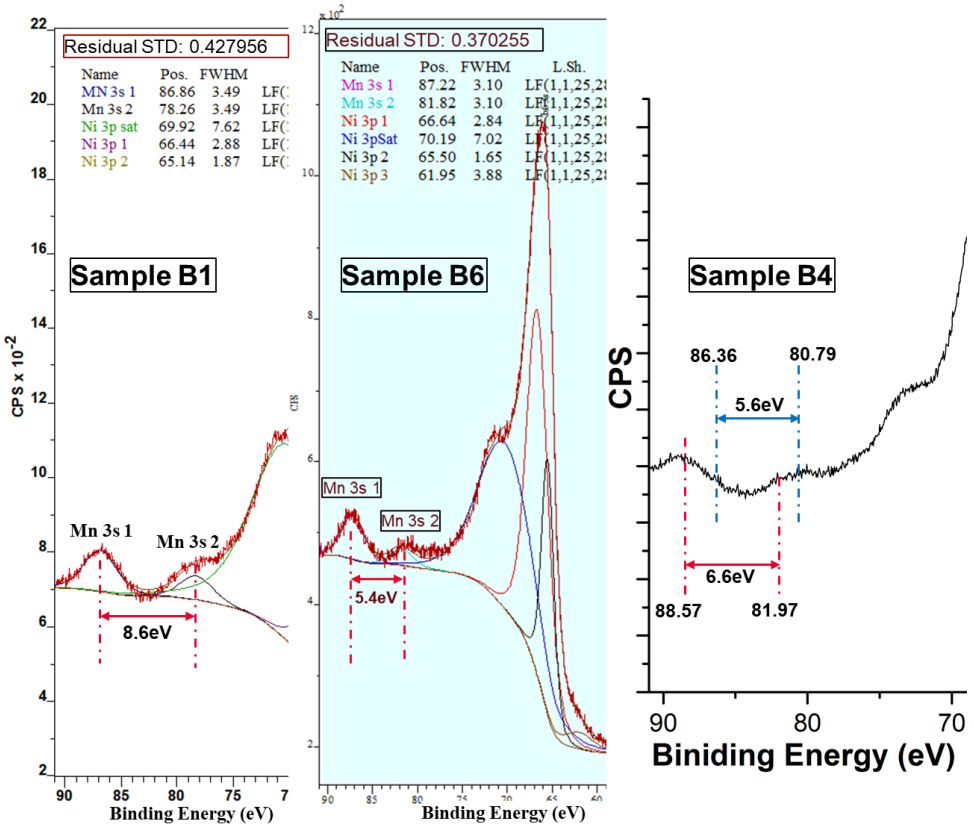

Figure 3.6: Multiplet splitting of Mn 3s XPS spectrum in different nanocrystal samples

Figure 3.7 reveals the peak fitting of O 1s XPS spectra for NiO nanoparticle (A1) and different other nanocrystals (B1, B3, and B7). The XPS spectra line for sample A1 consists of only two peaks, 529.22 eV and 530.81 eV of binding energy. According to the NIST database, the lower binding energy peak confirms the position of lattice oxygen, O^{2-} and the higher binding energy peak is for the HO-Ni-OH bond which occurs due to the hydroxylation process in aqueous synthesis medium. The nanocrystal samples have the Mn-O bond peak which occurs around 529±0.50 eV. Apparently, as the pH increases, the peak intensity for Mn-O is also increasing suggesting the Mn concentration is also going up. The amount of $Ni(OH)_2$ is varying due to the adhesion of hydroxyl ions over the surface of the nanocrystals and there is no definite trend for that with increasing pH value. For quantitative analysis, we have used the Ni $2p_{3/2}$, Mn $2p_{3/2}$ and O 1s region to get the percentage of all the elements. But the amount of $Ni(OH)_2$ has been excluded for quantitative analysis of the elements present in the samples. Table 3.5 shows the percentage amount of different elements in different nanocrystal samples.

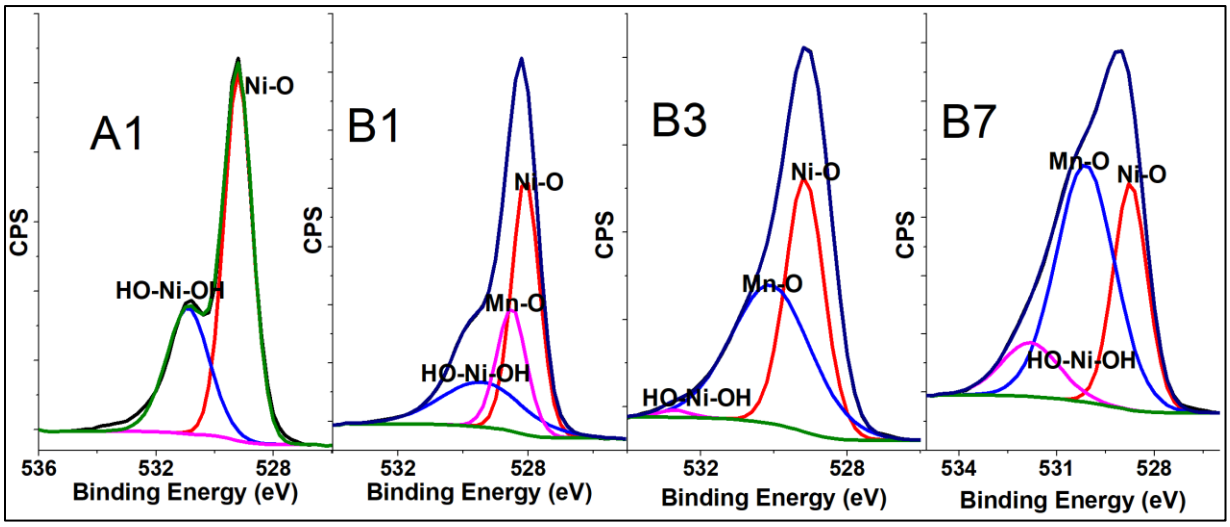

Figure 3.7: XPS spectra of O 1s region for NiO nanoparticle (A1) and nanocrystal samples

Table 3.5: percentage of elements derived from the quantitative analysis of XPS spectra

Name	B1	B2	B3	B4	B5	B6	B7	B8
Mn 2p 3/2	1.34	3.35	4.79	4.93	6.52	8.06	7.41	7.90
Ni 2p3/2 sat	16.22	17.36	15.45	15.32	16.38	14.04	13.28	16.17
Ni 2p3/2 sat	3.82	1.46	12.79	0.67	3.73	1.31	1.94	15.74
Ni 2p3/2	21.11	21.28	12.48	21.74	19.56	17.80	17.94	10.52
Ni 2p3/2	7.28	6.43	4.46	7.37	3.92	9.08	9.82	0.10
O 1s-Ni-O	32.18	32.20	36.59	32.08	31.84	33.49	28.33	41.31
O 1s Mn-O	18.05	17.91	13.44	17.88	18.04	16.21	21.28	8.26

As from table 3.5, we can see that the highest amount of Mn concentration is found in sample B6. The second-largest amount of Mn is in sample B8 followed by B7 and B5. Our magnetic data analysis has shown that the exchange bias and coercivity are also highest for sample B6 followed by sample B8, B7, and B5 among all other samples. Sample B6 occurs at a pH value of 5.03 which is the default pH value of the synthesis medium in the hydrothermal method when NiO nanoparticles are added to the $MnCl_2.3H_2O$ solution. As the pH of the samples is altered, the concentration of Mn is also changing. The lower pH values obstruct the adsorption of Mn ions which results in a lesser amount of Mn while at higher pH there are more Mn ions. The gradual increase of Mn ions up to B6 represents a similar pattern but again the decrease after B6 is arguable. We suspect that the reason behind the fallen trend of lower Mn values is related to the size of nanoislands in sample B7 and B8. As from TEM images, it is obvious that the nanoisland size is comparatively lower in B8 increasing the surface area of the overall sample. Since the surface area is increasing, XPS spectra are showing more prominent peaks at a higher intensity for sample B8 than B7.

Conclusion

Different kinds of NiO based nanocrystals samples were synthesized from pH 2.39 to 7.02 having Mn_3O_4 nanoislands and/or $Mn_xNi_{1-x}O$ shells. Our XRD and TEM data confirms the presence of more $Mn_xNi_{1-x}O$ shells in the lower pH value samples and more Mn_3O_4 nanoislands in higher pH values. The size of the Mn_3O_4 nanoislands can also vary with changing pH values. XPS spectra analysis manifests a similar outcome although the presence of Ni auger peaks makes the quantitative analysis challenging. Incorporation of NIST XPS data helps to overcome the challenge and successful interpretation of the results.

References

[1] E. C. Scher *et al.*, "Shape control and applications of nanocrystals," *Philos. Trans. R. Soc. A Math. Phys. Eng. Sci.*, vol. 361, no. 1803, pp. 241–257, 2003, doi: 10.1098/rsta.2002.1126.

[2] L. Carbone and P. D. Cozzoli, "Colloidal heterostructured nanocrystals: Synthesis and growth mechanisms," *Nano Today*, vol. 5, no. 5, pp. 449–493, 2010, doi: 10.1016/j.nantod.2010.08.006.

[3] P. D. Cozzoli and C. Nobile, *Colloidal oxide-based heterostructured nanocrystals*. Elsevier Inc., 2020.

[4] T. Zhu, S. G. Cloutier, I. Ivanov, K. L. Knappenberger, I. Robel, and F. Zhang, "Nanocrystals for electronic and optoelectronic applications," *J. Nanomater.*, vol. 2012, pp. 2012–2014, 2012, doi: 10.1155/2012/392742.

[5] Y. W. Jun, J. S. Choi, and J. Cheon, "Heterostructured magnetic nanoparticles: Their versatility and high performance capabilities," *Chem. Commun.*, no. 12, pp. 1203–1214, 2007, doi: 10.1039/b614735f.

[6] R. Scarfiello, C. Nobile, and P. D. Cozzoli, "Colloidal magnetic heterostructured nanocrystals with asymmetric topologies: Seeded-growth synthetic routes and formation mechanisms," *Front. Mater.*, vol. 3, no. December, pp. 1–29, 2016, doi:

10.3389/fmats.2016.00056.

[7] H. Zhong, T. Mirkovic, and G. D. Scholes, “Nanocrystal Synthesis,” *Compr. Nanosci. Technol.*, vol. 1–5, pp. 153–201, 2011, doi: 10.1016/B978-0-12-374396-1.00051-9.

[8] J. Liu, S. Z. Qiao, J. S. Chen, X. W. Lou, X. Xing, and G. Q. Lu, “Yolk/shell nanoparticles: New platforms for nanoreactors, drug delivery and lithium-ion batteries,” *Chem. Commun.*, vol. 47, no. 47, pp. 12578–12591, 2011, doi: 10.1039/c1cc13658e.

[9] P. Alivisatos, “The use of nanocrystals in biological detection,” *Nat. Biotechnol.*, vol. 22, no. 1, pp. 47–52, 2004, doi: 10.1038/nbt927.

[10] D. S, “Application of Nanocrystals in Drug Delivery: an Overview,” *Bull. Pharm. Res.*, vol. 8, no. 2, pp. 1–9, 2018, doi: 10.21276/bpr.2018.8.2.4.

[11] J. Gao, H. Gu, and B. Xu, “Multifunctional Magnetic Nanoparticles: Design, Synthesis, and Biomedical Applications,” *Acc. Chem. Res.*, vol. 42, no. 8, pp. 1097–1107, Aug. 2009, doi: 10.1021/ar9000026.

[12] K. Hermann and M. Witko, “Chapter 4 Theory of physical and chemical behavior of transition metal oxides: vanadium and molybdenum oxides,” *Chem. Phys. Solid Surfaces*, vol. 9, no. C, pp. 136–198, 2001, doi: 10.1016/S1571-0785(01)80024-9.

[13] B. Ramachandra, S. C. Jung, K. S. Kim, K. Y. Choo, J. S. Sung, and T. H. Kim, *MoVW-mixed oxide as a partial oxidation catalyst for methanol to formaldehyde*, vol. 159. Elsevier Masson SAS, 2006.

[14] A. L. Strickler, M. Escudero-Escribano, and T. F. Jaramillo, “Core-Shell Au@Metal-Oxide Nanoparticle Electrocatalysts for Enhanced Oxygen Evolution,” *Nano Lett.*, vol. 17, no. 10, pp. 6040–6046, 2017, doi: 10.1021/acs.nanolett.7b02357.

[15] S. E. Ahn *et al.*, “Write current reduction in transition metal oxide based resistance-change memory,” *Adv. Mater.*, vol. 20, no. 5, pp. 924–928, 2008, doi: 10.1002/adma.200702081.

[16] M. J. Lee *et al.*, “Electrical manipulation of nanofilaments in transition-metal oxides for resistance-based memory,” *Nano Lett.*, vol. 9, no. 4, pp. 1476–1481, 2009, doi: 10.1021/nl803387q.

[17] S. P. Pati, B. Bhushan, A. Basumallick, S. Kumar, and D. Das, “Exchange bias and suppression of superparamagnetism of α-Fe nanoparticles in NiO matrix,” *Mater. Sci. Eng. B Solid-State Mater. Adv. Technol.*, vol. 176, no. 13, pp. 1015–1020, 2011, doi: 10.1016/j.mseb.2011.05.019.

[18] V. Skumryev, S. Stoyanov, Y. Zhang, G. Hadjipanayis, D. Givord, and J. Nogués, “Beating the superparamagnetic limit with exchange bias,” *Nature*, vol. 423, no. 6942, pp. 850–853, 2003, doi: 10.1038/nature01687.

[19] W. Yan *et al.*, “Valence state-dependent ferromagnetism in Mn-doped NiO thin films,” *Adv. Mater.*, vol. 24, no. 3, pp. 353–357, 2012, doi: 10.1002/adma.201103436.

[20] J. Al Boukhari, L. Zeidan, A. Khalaf, and R. Awad, “Synthesis, characterization, optical and magnetic properties of pure and Mn, Fe and Zn doped NiO nanoparticles,” *Chem. Phys.*, vol. 516, pp. 116–124, 2019, doi: 10.1016/j.chemphys.2018.07.046.

[21] P. Mallick, C. Rath, A. Rath, A. Banerjee, and N. C. Mishra, “Antiferro to superparamagnetic transition on Mn doping in NiO,” *Solid State Commun.*, vol. 150, no. 29–30, pp. 1342–1345, 2010, doi: 10.1016/j.ssc.2010.05.003.

[22] S. Layek and H. C. Verma, “Room temperature ferromagnetism in Mn-doped NiO nanoparticles,” *J. Magn. Magn. Mater.*, vol. 397, pp. 73–78, 2016, doi: 10.1016/j.jmmm.2015.08.082.

[23] S. Hasan, R. A. Mayanovic, and M. Benamara, “Synthesis and Characterization of Novel Inverted NiO @ Ni x Mn 1-x O Core-Shell Nanoparticles,” *MRS Adv.*, vol. 2, no. 56, pp. 3465–3470, Jun. 2017, doi: 10.1557/adv.2017.445.

[24] M. D. Hossain, S. Dey, R. A. Mayanovic, and M. Benamara, “Structural and Magnetic Properties of Well-Ordered Inverted Core-Shell α-Cr 2 O 3 / α-M x Cr 2-x O 3 (M=Co, Ni, Mn, Fe) Nanoparticles,” *MRS Adv.*, vol. 1, no. 34, pp. 2387–2392, May 2016, doi: 10.1557/adv.2016.324.

[25] W. Zhan, C. Xu, G. Qian, G. Huang, X. Tang, and B. Lin, “Adsorption of Cu(ii), Zn(ii), and Pb(ii) from aqueous single and binary metal solutions by regenerated cellulose and sodium alginate chemically modified with polyethyleneimine,” *RSC Adv.*, vol. 8, no. 33, pp. 18723–18733, 2018, doi: 10.1039/c8ra02055h.

[26] E. A. Jenne, “Priorities for Future Metal Adsorption Research,” *Adsorpt. Met. by Geomedia*, no. 1989, pp. 549–560, 1998, doi: 10.1016/b978-012384245-9/50026-8.

[27] M. N. Zafar, R. Nadeem, and M. A. Hanif, “Biosorption of nickel from protonated rice bran,” *J. Hazard. Mater.*, vol. 143, no. 1–2, pp. 478–485, 2007, doi: 10.1016/j.jhazmat.2006.09.055.

[28] J. Guzmán, I. Saucedo, R. Navarro, J. Revilla, and E. Guibal, “Vanadium interactions with chitosan: Influence of polymer protonation and metal speciation,” *Langmuir*, vol. 18, no. 5, pp. 1567–1573, 2002, doi: 10.1021/la010802n.

[29] D. V. Bavykin, J. M. Friedrich, and F. C. Walsh, “Protonated titanates and TiO2 nanostructured materials: Synthesis, properties, and applications,” *Adv. Mater.*, vol. 18, no. 21, pp. 2807–2824, 2006, doi: 10.1002/adma.200502696.

[30] T. Sugimoto, “Formation of modoispersed nano- and micro-particles controlled in size, shape, and internal structure,” *Chem. Eng. Technol.*, vol. 26, no. 3, pp. 313–321, 2003, doi: 10.1002/ceat.200390048.

[31] S. Ghorbani Gorji, E. Ghorbani Gorji, and M. A. Mohammadifar, “Effect of pH on turbidity, size, viscosity and the shape of sodium caseinate aggregates with light scattering and rheometry,” *J. Food Sci. Technol.*, vol. 52, no. 3, pp. 1820–1824, 2015, doi: 10.1007/s13197-013-1144-2.

[32] J. P. Jolivet, S. Cassaignon, C. Chanéac, D. Chiche, O. Durupthy, and D. Portehault, “Design of metal oxide nanoparticles: Control of size, shape, crystalline structure and functionalization by aqueous chemistry,” *Comptes Rendus Chim.*, vol. 13, no. 1–2, pp. 40–51, 2010, doi: 10.1016/j.crci.2009.09.012.

[33] S. W. G. Naumkin, Alexander V., Anna Kraut-Vass, C. J. Powell, *NIST X-ray Photoelectron Spectroscopy Database*, 4.1. Measurement Services Division of the National Institute of Standards and Technology (NIST) Technology Services, 2012.

[34] M. El-Kemary, N. Nagy, and I. El-Mehasseb, “Nickel oxide nanoparticles: Synthesis and spectral studies of interactions with glucose,” *Mater. Sci. Semicond. Process.*, vol. 16, no. 6, pp. 1747–1752, 2013, doi: 10.1016/j.mssp.2013.05.018.

[35] M. D. Hossain, R. A. Mayanovic, R. Sakidja, and M. Benamara, “An experimental and theoretical study of the optical, electronic, and magnetic properties of novel inverted α-Cr2O3atα-Mn0.35Cr1.65O2.94 core shell nanoparticles,” *J. Mater. Res.*, vol. 32, no. 2, pp. 269–278, 2017, doi: 10.1557/jmr.2016.504.

[36] S. Dey, M. D. Hossain, R. A. Mayanovic, R. Wirth, and R. A. Gordon, “Novel highly

ordered core–shell nanoparticles," *J. Mater. Sci.*, vol. 52, no. 4, pp. 2066–2076, 2017, doi: 10.1007/s10853-016-0495-2.

[37] P. R. Garcês Gonçalves, H. A. De Abreu, and H. A. Duarte, "Stability, Structural, and Electronic Properties of Hausmannite (Mn3O4) Surfaces and Their Interaction with Water," *J. Phys. Chem. C*, vol. 122, no. 36, pp. 20841–20849, 2018, doi: 10.1021/acs.jpcc.8b06201.

[38] O. Y. Gorbenko *et al.*, "The structure and properties of Mn3O4 thin films grown by MOCVD," *Solid State Commun.*, vol. 124, no. 1–2, pp. 15–20, 2002, doi: 10.1016/S0038-1098(02)00470-2.

[39] C. A. BARRETT and E. B. EVANS, "Solid Solubility and Lattice Parameter of NiO-MnO," *J. Am. Ceram. Soc.*, vol. 47, no. 10, pp. 533–533, 1964, doi: 10.1111/j.1151-2916.1964.tb13806.x.

[40] Z. Swiatkowska-Warkocka *et al.*, "Tailoring of magnetic properties of nio/ni composite particles fabricated by pulsed laser irradiation," *Nanomaterials*, vol. 8, no. 10, 2018, doi: 10.3390/nano8100790.

[41] A. K. Chatterjee, "Handbook of Analytical Techniques in Concrete Science and Technology," *Handb. Anal. Tech. Concr. Sci. Technol.*, pp. 275–332, 2001, doi: 10.1016/B978-081551437-4.50011-4.

[42] P. Persson, S. Lunell, A. Szöke, B. Ziaja, and J. Hajdu, "Shake-up and shake-off excitations with associated electron losses in X-ray studies of proteins," *Protein Sci.*, vol. 10, no. 12, pp. 2480–2484, 2009, doi: 10.1110/ps.ps.26201.

[43] V. Biju and M. Abdul Khadar, "Electronic structure of nanostructured nickel oxide using Ni 2p XPS analysis," *J. Nanoparticle Res.*, vol. 4, no. 3, pp. 247–253, 2002, doi: 10.1023/A:1019949805751.

[44] D. Wilson and M. A. Langell, "XPS analysis of oleylamine/oleic acid capped Fe 3 O 4 nanoparticles as a function of temperature," *Appl. Surf. Sci.*, vol. 303, pp. 6–13, 2014, doi: 10.1016/j.apsusc.2014.02.006.

[45] M. C. Biesinger, B. P. Payne, A. P. Grosvenor, L. W. M. Lau, A. R. Gerson, and R. S. C. Smart, "Resolving surface chemical states in XPS analysis of first row transition metals, oxides and hydroxides: Cr, Mn, Fe, Co and Ni," *Appl. Surf. Sci.*, vol. 257, no. 7, pp. 2717–2730, 2011, doi: 10.1016/j.apsusc.2010.10.051.

[46] M. C. Biesinger, L. W. M. Lau, A. R. Gerson, and R. S. C. Smart, "The role of the Auger parameter in XPS studies of nickel metal, halides and oxides," *Phys. Chem. Chem. Phys.*, vol. 14, no. 7, pp. 2434–2442, 2012, doi: 10.1039/c2cp22419d.

[47] A. P. Grosvenor, M. C. Biesinger, R. S. C. Smart, and N. S. McIntyre, "New interpretations of XPS spectra of nickel metal and oxides," *Surf. Sci.*, vol. 600, no. 9, pp. 1771–1779, 2006, doi: 10.1016/j.susc.2006.01.041.

[48] M. C. Biesinger, B. P. Payne, L. W. M. Lau, A. Gerson, and R. S. C. Smart, "X-ray photoelectron spectroscopic chemical state Quantification of mixed nickel metal, oxide and hydroxide systems," *Surf. Interface Anal.*, vol. 41, no. 4, pp. 324–332, 2009, doi: 10.1002/sia.3026.

[49] M. A. Peck and M. A. Langell, "Comparison of nanoscaled and bulk NiO structural and environmental characteristics by XRD, XAFS, and XPS," *Chem. Mater.*, vol. 24, no. 23, pp. 4483–4490, 2012, doi: 10.1021/cm300739y.

[50] J. He *et al.*, "Hierarchical Mesoporous NiO/MnO2@PANI Core-Shell Microspheres, Highly Efficient and Stable Bifunctional Electrocatalysts for Oxygen Evolution and Reduction Reactions," *ACS Appl. Mater. Interfaces*, vol. 9, no. 49, pp. 42676–42687, 2017, doi: 10.1021/acsami.7b07383.

[51] Y. Jiang *et al.*, "Mn modified Ni/bentonite for CO 2 methanation," *Catalysts*, vol. 8, no. 12, 2018, doi: 10.3390/catal8120646.

[52] X. Li *et al.*, "Insight of synergistic effect of different active metal ions in layered double hydroxides on their electrochemical behaviors," *Electrochim. Acta*, vol. 253, no. September, pp. 302–310, 2017, doi: 10.1016/j.electacta.2017.09.075.

[53] J. M. Sanz and G. T. Tyuliev, "An XPS study of thin NiO films deposited on MgO(100)," *Surf. Sci.*, vol. 367, no. 2, pp. 196–202, 1996, doi: 10.1016/S0039-6028(96)00818-7.

[54] E. S. Ilton, J. E. Post, P. J. Heaney, F. T. Ling, and S. N. Kerisit, "XPS determination of Mn oxidation states in Mn (hydr)oxides," *Appl. Surf. Sci.*, vol. 366, pp. 475–485, 2016, doi: 10.1016/j.apsusc.2015.12.159.

[55] S. Xi, Y. Zhu, Y. Yang, S. Jiang, and Z. Tang, "Facile Synthesis of Free-Standing NiO/MnO2 Core-Shell Nanoflakes on Carbon Cloth for Flexible Supercapacitors," *Nanoscale Res. Lett.*, vol. 12, no. 1, 2017, doi: 10.1186/s11671-017-1939-6.

[56] V. R. Galakhov *et al.*, "Mn (formula presented) exchange splitting in mixed-valence manganites," *Phys. Rev. B - Condens. Matter Mater. Phys.*, vol. 65, no. 11, pp. 1–4, 2002, doi: 10.1103/PhysRevB.65.113102.

[57] M. Yang *et al.*, "Mn3O4-NiO-Ni/CNTs catalysts prepared by spontaneous redox at high temperature and their superior catalytic performance in selective oxidation of benzyl alcohol," *J. Mol. Catal. A Chem.*, vol. 380, pp. 61–69, 2013, doi: 10.1016/j.molcata.2013.09.011.

[58] A. K. Shukla, P. Krüger, R. S. Dhaka, D. I. Sayago, K. Horn, and S. R. Barman, "Understanding the 2p core-level spectra of manganese: Photoelectron spectroscopy experiments and Anderson impurity model calculations," *Phys. Rev. B - Condens. Matter Mater. Phys.*, vol. 75, no. 23, pp. 1–6, 2007, doi: 10.1103/PhysRevB.75.235419.

[59] M. C. Biesinger, B. P. Payne, A. P. Grosvenor, L. W. M. Lau, A. R. Gerson, and R. S. C. Smart, "Resolving surface chemical states in XPS analysis of first row transition metals, oxides and hydroxides: Cr, Mn, Fe, Co and Ni," *Appl. Surf. Sci.*, vol. 257, no. 7, pp. 2717–2730, 2011, doi: 10.1016/j.apsusc.2010.10.051.

[60] L. Sangaletti, F. Parmigiani, and P. S. Bagus, "Sum rule to evaluate the exchange energy in core-level photoemission," *Phys. Rev. B - Condens. Matter Mater. Phys.*, vol. 66, no. 11, pp. 1151061–1151067, 2002, doi: 10.1103/PhysRevB.66.115106.

[61] P. S. Bagus, R. Broer, and E. S. Ilton, "Atomic near-degeneracy for photoemission: Generality of 4f excitations," *J. Electron Spectros. Relat. Phenomena*, vol. 165, no. 1–3, pp. 46–49, 2008, doi: 10.1016/j.elspec.2008.07.008.

[62] S. Ardizzone, C. L. Bianchi, and D. Tirelli, "Mn3O4 and γ-MnOOH powders, preparation, phase composition and XPS characterisation," *Colloids Surfaces A Physicochem. Eng. Asp.*, vol. 134, no. 3, pp. 305–312, 1998, doi: 10.1016/S0927-7757(97)00219-7.

[63] J. L. Junta and M. F. Hochella, "Manganese (II) oxidation at mineral surfaces: A microscopic and spectroscopic study," *Geochim. Cosmochim. Acta*, vol. 58, no. 22, pp. 4985–4999, 1994, doi: 10.1016/0016-7037(94)90226-7.

[64] A. J. Nelson, J. G. Reynolds, and J. W. Roos, "Core-level satellites and outer core-level multiplet splitting in Mn model compounds," *J. Vac. Sci. Technol. A Vacuum, Surfaces, Film.*, vol. 18, no. 4, pp. 1072–1076, 2000, doi: 10.1116/1.582302.

SUMMARY

The present study deals with the effect of pH used in hydrothermal synthesis on the structural and magnetic properties of NiO-based bimagnetic heterostructured nanocrystals (MHNCs). The NiO core nanoparticles were synthesized via thermal decomposition whereas the $Mn_xNi_{1-x}O$ and/or Mn_3O_4 outer nanophases were synthesized using a low-temperature hydrothermal method. The pH of the hydrothermal synthesis medium was varied from 2.4 to 7.0. The amount of pH is found to directly affect the type and thickness/size of the shell layer as well as the morphology of the magnetic nanocrystals. XRD spectral analysis and Rietveld refinement confirm the presence of the $Mn_xNi_{1-x}O$ shell layer and/or Mn_3O_4 decorating islands and indicate a trend of the relative amount of each of these phases covering the NiO core. The results from the TEM, XPS, and MPMS magnetic characterization show a transition from $Mn_xNi_{1-x}O$ shell at lower pH values to a mixed $Mn_xNi_{1-x}O$ and Mn_3O_4 coverage at medium range pH values, and finally to Mn_3O_4 (predominantly) overgrowth on NiO core nanoparticles at higher pH values. A considerable increase in saturation and remanent magnetization, as well as magnetic coercivity, is observed for the MHNCs synthesized at the middle range of pH values (~ 4 – 6 range) confirming the initial hypothesis that acidic but trending toward neutral pH values favor the deposition of manganese oxides. Mn_3O_4 has a high FiM magnetic anisotropy energy resulting from their crystal structure and misalignments at the interface of the structure along with the vacancies and stacking faults. In addition, the nanocrystals containing Mn_3O_4 showed a significant enhancement in exchange bias peaking at a pH of ~5. This is consistent with the XRD and TEM results showing a higher amount of Mn_3O_4 at a pH of ~4.5 – 7. The decrease of exchange bias after pH ~5 can be attributed to the reduction of Mn_3O_4 nanoisland size. Magnetic

data also shows a trend in magnetic domain formation at different pH values. Multiple magnetic domain formation is observed at a pH value of ~2.5 – 3 while single domains are dominant in the upper pH value of ~6 – 7. There is also a pseudo-domain type magnetic formation at an intermittent pH value of ~3.5 – 5 showing different features of both single and multiple domains. The XPS results show good comparison with other characterization methods in terms of the manganese oxidation states and the percentage of manganese oxides. One simple method which primarily concentrates on pure NiO LMM Auger peak fitting and then uses the same data to fit Mn $2p_{3/2}$ peaks generates very good result to solve the peak mixing problem between the two elements (Ni and Mn). The oxidation states of manganese oxide are first identified from the binding energy difference of Mn $2p_{1/2}$ and Mn $2p_{3/2}$ peaks following this simple observation method. A fair amount of multiplet splitting is also observed in the Mn 3s region where the energy difference between the two multiplet peaks reconfirms the data seen from Mn $2p_{1/2}$ and Mn $2p_{3/2}$ peak observation. Both of the spectrum analysis gives the same consistent data that only $Mn_xNi_{1-x}O$ shell layer forms at pH ~2.4, both $Mn_xNi_{1-x}O$ shell and Mn_3O_4 islands form at pH ~3 – 4 and Mn_3O_4 islands forms at pH ~4.5 –7. The quantitative analysis of the XPS data exhibits a higher amount of Mn concentration for pH ~5 –7 which is also consistent with XRD data.

REFERENCES

[1] Y. Xia, Y. Xiong, B. Lim, and S. E. Skrabalak, "Shape-Controlled Synthesis of Metal Nanocrystals : Simple," *Angew. Chemie Int. Ed.*, vol. 48, no. 1, pp. 60–103, 2009, doi: 10.1002/anie.200802248.Shape-Controlled.

[2] D. Shi, Z. Guo, and N. Bedford, "Nanocomposites," in *Nanomaterials and Devices*, vol. 15, no. 5, Elsevier, 2015, pp. 293–315.

[3] R. C. Ashoori, "Electrons in artificial atoms," *Nature*, vol. 379, no. 6564, pp. 413–419, 1996, doi: 10.1038/379413a0.

[4] M. Vert *et al.*, "Terminology for biorelated polymers and applications (IUPAC Recommendations 2012)," *Pure Appl. Chem.*, vol. 84, no. 2, pp. 377–410, Jan. 2012, doi: 10.1351/PAC-REC-10-12-04.

[5] B. O'Regan and M. Grätzel, "A low-cost, high-efficiency solar cell based on dye-sensitized colloidal TiO2 films," *Nature*, vol. 353, no. 6346, pp. 737–740, 1991, doi: 10.1038/353737a0.

[6] H. Zabel, "Magnetic heterostructures: Examples and perspectives," *Philos. Mag. B Phys. Condens. Matter; Stat. Mech. Electron. Opt. Magn. Prop.*, vol. 80, no. 2, pp. 293–306, 2000, doi: 10.1080/13642810008208617.

[7] S. V. P. Vattikuti, *Heterostructured Nanomaterials: Latest Trends in Formation of Inorganic Heterostructures*, no. i. Elsevier Ltd., 2018.

[8] M. Gibertini, M. Koperski, A. F. Morpurgo, and K. S. Novoselov, "Magnetic 2D materials and heterostructures," *Nat. Nanotechnol.*, vol. 14, no. 5, pp. 408–419, 2019, doi: 10.1038/s41565-019-0438-6.

[9] Y. W. Jun, J. S. Choi, and J. Cheon, "Heterostructured magnetic nanoparticles: Their versatility and high performance capabilities," *Chem. Commun.*, no. 12, pp. 1203–1214, 2007, doi: 10.1039/b614735f.

[10] T. Markvart and L. Castañer, "Principles of Solar Cell Operation," in *Solar Cells*, Elsevier, 2013, pp. 3–25.

[11] P. Capper, S. Irvine, and T. Joyce, “Epitaxial Crystal Growth: Methods and Materials,” in *Springer Handbook of Electronic and Photonic Materials*, S. Kasap and P. Capper, Eds. Cham: Springer International Publishing, 2017, p. 1.

[12] J. Zhang, “Nonepitaxial Growth of Hybrid,” *Science*, vol. 1634, no. March, pp. 1634–1639, 2012, doi: 10.1126/science.1184769.

[13] S. E. Wawra, L. Pflug, T. Thajudeen, C. Kryschi, M. Stingl, and W. Peukert, “Determination of the two-dimensional distributions of gold nanorods by multiwavelength analytical ultracentrifugation,” *Nat. Commun.*, vol. 9, no. 1, p. 4898, 2018, doi: 10.1038/s41467-018-07366-9.

[14] Y. Liang *et al.*, “Symmetry control of nanorod superlattice driven by a governing force,” *Nat. Commun.*, vol. 8, no. 1, p. 1410, 2017, doi: 10.1038/s41467-017-01111-4.

[15] A. Abdulkareem Ghassan, N. Mijan, and Y. Hin Taufiq-Yap, “Nanomaterials: An Overview of Nanorods Synthesis and Optimization,” in *Nanorods and Nanocomposites*, IntechOpen, 2020, pp. 1–24.

[16] Z. Zhong, C. Yang, and C. M. Lieber, “SILICON NANOWIRES AND NANOWIRE HETEROSTRUCTURES,” in *Nanosilicon*, Elsevier, 2008, pp. 176–216.

[17] X. Chen, D. Peng, Q. Ju, and F. Wang, “Photon upconversion in core-shell nanoparticles,” *Chem. Soc. Rev.*, vol. 44, no. 6, pp. 1318–1330, 2015, doi: 10.1039/c4cs00151f.

[18] R. Scarfiello, C. Nobile, and P. D. Cozzoli, “Colloidal magnetic heterostructured nanocrystals with asymmetric topologies: Seeded-growth synthetic routes and formation mechanisms,” *Front. Mater.*, vol. 3, no. December, pp. 1–29, 2016, doi: 10.3389/fmats.2016.00056.

[19] M. Estrader *et al.*, “Robust antiferromagnetic coupling in hard-soft bi-magnetic core/shell nanoparticles,” *Nat. Commun.*, vol. 4, pp. 1–8, 2013, doi: 10.1038/ncomms3960.

[20] G. Lavorato *et al.*, “Exchange bias and surface effects in bimagnetic CoO-core/Co0.5Ni0.5Fe2 O4 -shell nanoparticles,” *Phys. Rev. B*, vol. 94, no. 5, pp. 1–9, 2016, doi: 10.1103/PhysRevB.94.054432.

[21] T. Okada *et al.*, “Magnetic and electronic properties of bimagnetic materials comprising cobalt particles within hollow silica decorated with magnetite nanoparticles,” *J. Appl.*

Phys., vol. 114, no. 12, 2013, doi: 10.1063/1.4822299.

[22] A. S. Antonov and N. A. Buznikov, "Asymmetric magnetoimpedance in two-phase ferromagnetic film structures," *Tech. Phys. Lett.*, vol. 42, no. 8, pp. 814–817, 2016, doi: 10.1134/S1063785016080034.

[23] A. K. Cheetham and D. A. O. Hope, "Magnetic ordering and exchange effects in the antiferromagnetic solid solutions MnxNi1-xO," *Phys. Rev. B*, vol. 27, no. 11, pp. 6964–6967, 1983, doi: 10.1103/PhysRevB.27.6964.

[24] S. Ardizzone, C. L. Bianchi, and D. Tirelli, "Mn3O4 and γ-MnOOH powders, preparation, phase composition and XPS characterisation," *Colloids Surfaces A Physicochem. Eng. Asp.*, vol. 134, no. 3, pp. 305–312, 1998, doi: 10.1016/S0927-7757(97)00219-7.

[25] H. Zabel and S. D. Bader, *Magnetic Heterostructures*, vol. 227, no. 5. Berlin, Heidelberg: Springer Berlin Heidelberg, 2008.

[26] A. Lopez-Ortega *et al.*, "Size-dependent passivation shell and magnetic properties in antiferromagnetic/ferrimagnetic core/shell MnO nanoparticles," *J. Am. Chem. Soc.*, vol. 132, no. 27, pp. 9398–9407, 2010, doi: 10.1021/ja1021798.

[27] A. Silva *et al.*, "Magnetic Particles in Biotechnology: From Drug Targeting to Tissue Engineering," in *Advances in Applied Biotechnology*, vol. i, no. tourism, InTech, 2012, p. 13.

[28] Y. X. Wang *et al.*, "Outstanding Comprehensive Performance of La(Fe, Si)13Hy/In Composite with Durable Service Life for Magnetic Refrigeration," *Adv. Electron. Mater.*, vol. 4, no. 5, pp. 1–8, 2018, doi: 10.1002/aelm.201700636.

[29] N. J. Borys, M. J. Walter, J. Huang, D. V. Talapin, and J. M. Lupton, "The Role of Particle Morphology in Interfacial Energy Transfer in CdSe/CdS Heterostructure Nanocrystals," *Science (80-.).*, vol. 330, no. 6009, pp. 1371–1374, Dec. 2010, doi: 10.1126/science.1198070.

[30] C. P. Byers *et al.*, "From tunable core-shell nanoparticles to plasmonic drawbridges: Active control of nanoparticle optical properties," *Sci. Adv.*, vol. 1, no. 11, pp. 1–10, 2015, doi: 10.1126/sciadv.1500988.

[31] K. Chatterjee, S. Sarkar, K. Jagajjanani Rao, and S. Paria, "Core/shell nanoparticles in

biomedical applications," *Adv. Colloid Interface Sci.*, vol. 209, pp. 8–39, Jul. 2014, doi: 10.1016/j.cis.2013.12.008.

[32] A. Chakraborty, "Effects of nanoscale inhomogeneities on the magnetic properties of diluted magnetic systems," no. October, 2016.

[33] M. Tadic, D. Nikolic, M. Panjan, and G. R. Blake, "Magnetic properties of NiO (nickel oxide) nanoparticles: Blocking temperature and Néel temperature," *J. Alloys Compd.*, vol. 647, pp. 1061–1068, 2015, doi: 10.1016/j.jallcom.2015.06.027.

[34] R. H. Kodama, S. A. Makhlouf, and A. E. Berkowitz, "Finite Size Effects in Antiferromagnetic NiO Nanoparticles," *Phys. Rev. Lett.*, vol. 79, no. 7, pp. 1393–1396, Aug. 1997, doi: 10.1103/PhysRevLett.79.1393.

[35] David Hemmendinger, "Computer memory," *Encyclopædia Britannica*. Encyclopædia Britannica, inc.

[36] M. Castell and P. Wincott, "Atomic-resolution STM of a system with strongly correlated electrons:NiO(001) surface structure and defect sites," *Phys. Rev. B - Condens. Matter Mater. Phys.*, vol. 55, no. 12, pp. 7859–7863, 1997, doi: 10.1103/PhysRevB.55.7859.

[37] A. J. Cinthia, R. Rajeswarapalanichamy, and K. Iyakutti, "First principles study of electronic structure, magnetic, and mechanical properties of transition metal monoxides TMO(TM=Co and Ni)," *Zeitschrift fur Naturforsch. - Sect. A J. Phys. Sci.*, vol. 70, no. 10, pp. 797–804, 2015, doi: 10.1515/zna-2015-0216.

[38] H. Momida and T. Oguchi, "First-principles studies of antiferromagnetic MnO and NiO surfaces," *J. Phys. Soc. Japan*, vol. 72, no. 3, pp. 588–593, 2003, doi: 10.1143/JPSJ.72.588.

[39] S. Hirai, Y. Goto, A. Wakatsuki, Y. Kamihara, M. Matoba, and W. L. Mao, "Electronic structure of spin frustrated magnets: Mn$_3$O$_4$ spinel and postspinel," vol. 3, pp. 1–6, 2014.

[40] W. H. Meiklejohn and C. P. Bean, "New Magnetic Anisotropy," *Phys. Rev.*, vol. 102, no. 5, pp. 1413–1414, Jun. 1956, doi: 10.1103/PhysRev.102.1413.

[41] E. C. STONER and E. P. WOHLFARTH, "Interpretation of High Coercivity in Ferromagnetic Materials," *Nature*, vol. 160, no. 4071, pp. 650–651, 1947, doi:

10.1038/160650a0.

[42] W. H. Meiklejohn and C. P. Bean, “New Magnetic Anisotropy,” *Phys. Rev.*, vol. 105, no. 3, pp. 904–913, Feb. 1957, doi: 10.1103/PhysRev.105.904.

[43] F. Radu, A. Westphalen, K. Theis-Bröhl, and H. Zabel, “Quantitative description of the azimuthal dependence of the exchange bias effect,” *J. Phys. Condens. Matter*, vol. 18, no. 3, pp. L29–L36, Dec. 2005, doi: 10.1088/0953-8984/18/3/l01.

[44] A. P. Malozemoff, “Random-field model of exchange anisotropy at rough ferromagnetic-antiferromagnetic interfaces,” *Phys. Rev. B*, vol. 35, no. 7, pp. 3679–3682, Mar. 1987, doi: 10.1103/PhysRevB.35.3679.

[45] U. Nowak, K. D. Usadel, J. Keller, P. Miltényi, B. Beschoten, and G. Güntherodt, “Domain state model for exchange bias. I. Theory,” *Phys. Rev. B - Condens. Matter Mater. Phys.*, vol. 66, no. 1, pp. 1–9, 2002, doi: 10.1103/PhysRevB.66.014430.

[46] M. F. Khan *et al.*, “Sol-gel synthesis of thorn-like ZnO nanoparticles endorsing mechanical stirring effect and their antimicrobial activities: Potential role as nano-antibiotics,” *Sci. Rep.*, vol. 6, no. 1, p. 27689, 2016, doi: 10.1038/srep27689.

[47] S. Hasan, R. A. Mayanovic, and M. Benamara, “Synthesis and Characterization of Novel Inverted NiO @ Ni x Mn 1-x O Core-Shell Nanoparticles,” *MRS Adv.*, vol. 2, no. 56, pp. 3465–3470, Jun. 2017, doi: 10.1557/adv.2017.445.

[48] M. D. Hossain, R. A. Mayanovic, R. Sakidja, M. Benamara, and R. Wirth, “Magnetic properties of core-shell nanoparticles possessing a novel Fe(II)-chromia phase: An experimental and theoretical approach,” *Nanoscale*, vol. 10, no. 4, pp. 2138–2147, 2018, doi: 10.1039/c7nr04770c.